

iToF2dTof: A Robust and Flexible Representation for Data-Driven Time-of-Flight Imaging

Felipe Gutierrez-Barragan^{*1,2}, Huaijin Chen¹, Mohit Gupta², Andreas Velten², and Jinwei Gu¹

¹SenseBrain Technology

²University of Wisconsin-Madison

Abstract—Indirect Time-of-Flight (iTof) cameras are a promising depth sensing technology. However, they are prone to errors caused by multi-path interference (MPI) and low signal-to-noise ratio (SNR). Traditional methods, after denoising, mitigate MPI by estimating a transient image that encodes depths. Recently, data-driven methods that jointly denoise and mitigate MPI have become state-of-the-art without using the intermediate transient representation. In this paper, we propose to revisit the transient representation. Using data-driven priors, we interpolate/extrapolate iTof frequencies and use them to estimate the transient image. Given direct ToF (dTof) sensors capture transient images, we name our method iTof2dTof. The transient representation is flexible. It can be integrated with different rule-based depth sensing algorithms that are robust to low SNR and can deal with ambiguous scenarios that arise in practice (e.g., specular MPI, optical cross-talk). We demonstrate the benefits of iTof2dTof over previous methods in real depth sensing scenarios.

Index Terms—depth sensing, time-of-flight.

I. INTRODUCTION

Indirect Time-of-Flight (iTof) imaging systems measure depths by illuminating the scene with a time-varying periodic signal, and computing the time-shift of the reflected signal [4]. iTof cameras can achieve high-resolution, while maintaining low-cost, small size and low power consumption, making them a popular choice, especially in resource constrained applications (e.g., Kinect for AR/VR).

Despite these strengths, iTof sensors face several practical challenges; namely, multi-path interference (MPI), and low signal-to-noise ratio (SNR). MPI arises from the indirect light paths captured by each pixel, which may cause strong depth errors. For example, points in a concave object may appear farther away, and specular objects or optical cross-talk can cause erroneous depth measurements. Low SNR, on the other hand, occurs when operated with low exposure times to reduce motion blur and power consumption [5]. Overall, practical solutions to MPI and low SNR are critical for emerging iTof-based 3D applications.

Recently, data-driven methods that jointly denoise and correct MPI errors, have been proposed [3], [6]–[9]. These solutions do not rely on additional hardware or long acquisition times, making them compact and low-power. Furthermore,

it is possible to implement them in real-time using light-weight neural networks [6], or through model compression and inference acceleration [10], [11].

Current data-driven models for iTof cameras perform supervision on the final depthmap representation during training. This approach works well when the training dataset provides *explicit supervision* for each depth sensing scenario that may arise. Explicit supervision is sometimes not available in scenarios that are challenging to simulate or capture ground truth (e.g., optical cross-talk), or in ambiguous scenarios, like sparse MPI, where the iTof data can encode multiple distances (e.g., specular or transparent surfaces, and depth discontinuities). The lack of such explicit supervision for each scenario can impact the generalization of the model.

In this paper, we propose an alternative output representation for data-driven iTof models. Similar to previous work, we input sparse iTof frequency measurements to the data-driven model. Different from previous approaches, our model outputs interpolated/extrapolated frequencies, on which supervision is performed. The estimated frequency data is used to estimate dToF/transient¹ images; therefore, the proposed method is called iTof2dTof. The dToF representation benefits from the data-driven model’s denoising capabilities, and continues to mitigate MPI by separating the direct and indirect illumination [12]. Furthermore, the data-driven model does not require explicit supervision on each depth sensing scenario because it only reconstructs the per-pixel dToF waveforms that encode distances in their peaks. To estimate depths, iTof2dTof is integrated with simple rule-based peak finding algorithms. Specifically,

- 1) Integrating iTof2dTof with a max peak finding algorithm results in *robust* depth sensing even at low SNR. This design is motivated by its relation to a recent depth decoding method for iTof [2] and structured light [13].
- 2) The *flexible* dToF representation allows us to design simple rule-based algorithms for challenging scenarios, like specular MPI and optical cross-talk, without re-training networks or increasing dataset size.

To summarize, our contributions are:

- A robust and flexible representation for data-driven iTof that improves depth sensing in different scenarios.
- An extensive validation of our data-driven models on real-world data with ground truth.
- A synthetic iTof dataset with realistic geometry, textures, and noise. The dataset will be released upon acceptance.

¹We use the terms dToF image and transient image interchangeably.

*Work done during internship at SenseBrain Technology

FGB, AV, and MG ({fgutierrez3, velten}@wisc.edu, mohitg@cs.wisc.edu) are with the University of Wisconsin-Madison, Madison, WI 53706. HC and JG ({chenhuaijin, gujinwei}@sensebrain.site) are with SenseBrain Technology, San Jose, CA 95131.

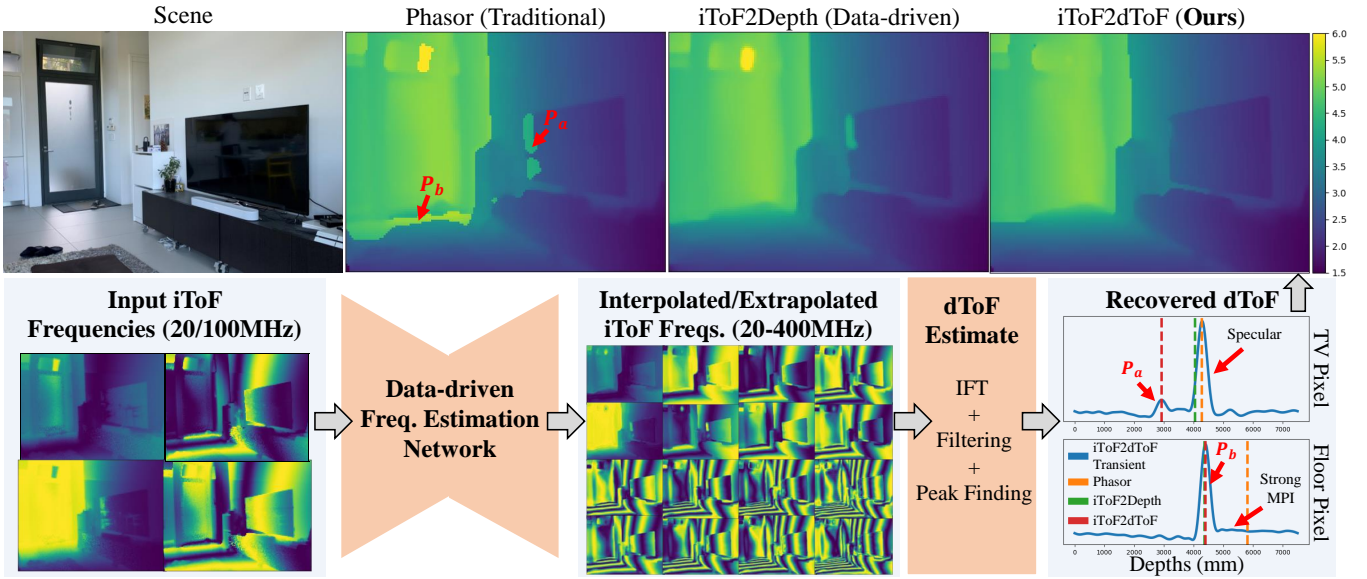


Fig. 1: **iToF2dToF**. We compare the iToF-based depth estimation results of previous traditional (Phasor [1], [2]) and data-driven (iTof2Depth [3]) approaches with our proposed data-driven method, iTof2dToF. Previous data-driven approaches map iToF data directly to depths making it hard to adapt to new scenarios such as specular MPI (e.g., TV Pixels). In iTof2dToF we interpolate/extrapolate the captured iToF frequencies and use them to estimate the transient image of the scene. Using rule-based peak finding algorithms, iTof2dToF, produces higher quality depth maps than previous solutions.

II. RELATED WORK

Mitigating MPI and recovering reliable depths from low SNR measurements are problems that have been extensively studied in the iToF literature [2], [14]–[21]. In this paper, we focus on solutions that could be applied to commercial iToF cameras without hardware modifications.

A. Transient Imaging

A *transient image* visualizes a light pulse propagating through a scene [22], where each pixel stores an intensity time profile, referred as a *transient pixel*. Usually, a transient pixel encodes depth as the first or max peak [12]. dToF systems capture transient images [23]–[25], enabling accurate depth reconstruction in many scenarios [26]–[29].

iToF Transient Imaging: Typical iToF systems sample temporal frequencies from the Fourier Transform of the scene’s transient image [30]. A large number of frequencies are required to recover a transient image. Therefore, to greatly reduce the number of measurements, iToF image formation models make strong assumptions on the transient structure. Previous work can be divided in two categories:

- **Sparse Transient Imaging:** One common approach assumes a sparse K -path model where each transient pixel is the sum of K delta functions, one for each light path. Both analytical [31]–[33] and numerical [34]–[37] solutions have been proposed. However, when $K \geq 3$, these methods require many measurements resulting in long acquisition times and high-power consumption.
- **Non-Sparse Transient Imaging:** Another family of methods relaxes the sparsity assumption on the transient image, but requires dense frequency sampling. Heide et al. [38]

fitted a parametric model to each transient pixel. Through Fourier analysis, Lin et al. [30], [39], recovered a transient image. More recently, [40] used a wavelet-based framework that achieved state-of-the-art accuracy, albeit at a higher computational cost. Peters et al. [33] proposed a real-time transient reconstruction algorithm that requires as few as 3 frequencies. However, it requires frame averaging due to its sensitivity to noise [40].

In this paper we introduce a data-driven non-sparse iToF transient imaging approach for the extreme case where only 2 frequencies are measured.

B. Data-driven ToF Imaging

Transient rendering [41]–[43] has enabled the simulation of ToF datasets, which has been essential for data-driven iToF due to the unavailability of real-world datasets with ground truth. Broadly, previous data-driven iToF models have used two types of “Input2Output” representations: Depth2Depth [6], [8], [9], [44] and iTof2Depth [3], [7]. Depth2Depth models take as input noisy and MPI-corrupted iToF depth images obtained from one [6] or multiple frequencies [8], [9], [44]. iTof2Depth models take as input raw multi-frequency iToF measurements with minimal pre-processing. Although, a variety of network architectures have been explored for these “Input2Output” representations (U-net [3], [6], coarse-to-fine CNN [8], [44], and KPN [7], [9], supervision has only been done on the output depth images. In this paper, we propose a different “Input2Output” representation (i.e., iTof2dToF) where the output, on which supervision is performed, are frequency-domain dToF images.

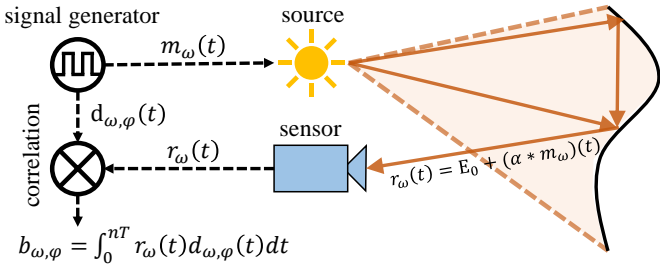


Fig. 2: **iToF Imaging.** The scene is flash illuminated with an amplitude modulated signal $m_\omega(t)$. The radiance, $r_\omega(t)$, arriving at each pixel is the sum of $m_\omega(t)$ over different light paths. At each pixel, $r_\omega(t)$ is correlated with a demodulation function, $d_{\omega,\varphi}(t)$. The product is integrated for an exposure time nT and the resulting intensity, $b_{\omega,\varphi}$, is recorded.

III. IMAGE FORMATION MODEL

Let $\alpha(x, y, t)$ be the transient image of a flash illuminated scene (Figure 2), where $\alpha(x, y, t)$ is the intensity of pixel (x, y) at time t . We will consider each transient pixel independently so we drop x and y . The domain of $\alpha(t)$ is on the nanosecond/picosecond scale, and $\alpha(t) \geq 0$ for all t .

ToF systems consist of a light source whose intensity is modulated with a periodic function $m_\omega(t)$ with period T . Here $\omega = 2\pi f$ where f is the repetition frequency. We assume that T is chosen such that all interesting light paths in $\alpha(t)$ happen at $t < T$, i.e., $\alpha(t) = 0$ for $t \geq T$. This assumption is necessary because we cannot recover the general aperiodic form of $\alpha(t)$ [33].

As illustrated in Figure 2, light propagates to the scene and returns to the sensor along different paths. The radiance incident on the sensor will be the convolution of $m_\omega(t)$ and the transient response of the scene, with a constant offset E_0 due to ambient light:

$$r_\omega(t) = E_0 + \int_0^\infty \alpha(\tau)m_\omega(t - \tau)d\tau = E_0 + (\alpha * m_\omega)(t) \quad (1)$$

A dToF system, measures $\alpha(t)$ using a delta-train modulation signal and sampling $r_\omega(t)$ with a high-speed sensor.

In iToF cameras, $r_\omega(t)$ is correlated with the sensor's periodic demodulation function, $d_{\omega,\varphi}(t)$, where φ is a controllable phase shift. Generally, the correlation is done by modulating the pixel gain according to $d_{\omega,\varphi}(t)$. In practice, one way to achieve this, is with dual-tap demodulation pixels [4], [45] that re-direct the photo-current between two buckets according to $d_{\omega,\varphi}(t)$. We model $d_{\omega,\varphi}(t)$ as zero-mean, which is achieved by taking the difference between the two buckets. The measured brightness for an exposure time, nT , would be,

$$b_{\omega,\varphi} = \int_0^{nT} r_\omega(t)d_{\omega,\varphi}(t)dt \quad (2)$$

Constants in Equation 2 cancel since $d_{\omega,\varphi}(t)$ is zero-mean.

A. Frequency Sampling with iToF Cameras

In most iToF systems $m_\omega(t)$ and $d_{\omega,\varphi}(t)$ are band-limited square functions, modelled as sinusoids. If we write $\alpha(t)$ as its Fourier Series between $[0, T]$, then $r_\omega(t)$ becomes:

$$\begin{aligned} r_\omega(t) &= E_0 + \alpha(t) * (P \cos(\omega t) + P) \\ &= E_0 + \sum_{k=0}^K A_{\omega_k} e^{i(\omega_k t - \phi_{\omega_k})} * (P \cos(\omega t) + P) \\ &= A_\omega \cos(\omega t - \phi_\omega) + L \end{aligned}$$

where $\omega_k = \omega k$, k is an integer, P is the average power, $L = E_0 + P \int_0^T \alpha(t)dt$ is a constant, and A_ω, ϕ_ω depend on the superposition of the returning sinusoids over all optical paths. In theory, K can be infinite, but in practice it depends on the time discretization. If we take two measurements with $d_{\omega,0}(t) = \cos(\omega t)$ and $d_{\omega,\frac{\pi}{2}}(t) = \sin(\omega t)$, we get the following brightness measurements:

$$b_{\omega,0} = \frac{A_\omega}{2} \cos(\phi_\omega), \quad b_{\omega,\frac{\pi}{2}} = \frac{A_\omega}{2} \sin(\phi_\omega) \quad (3)$$

In the simple case where the sensor only receives direct illumination, i.e., $\alpha(t) = \delta(t - \frac{2d}{c})$, ϕ_ω encodes depth as:

$$\phi_\omega = \frac{2\omega d}{c} \quad (4)$$

However, in the presence of MPI Equation 4 will give the incorrect depth.

Multi-frequency Sampling: By repeating the measurements in Equation 3 at different ω_k for $k = [1\dots K]$, we can recover $(A_{\omega_k}, \phi_{\omega_k})$. In other words, $\alpha(t)$ is reconstructed by measuring its Fourier coefficients. Since $\alpha(t)$ is computed for $t < T$ the maximum recoverable depth is $d_{\max} = \frac{cT}{2}$.

IV. THE iTof2DToF FRAMEWORK

Current iToF cameras are limited to sampling 2-3 frequencies, where the largest frequency is around 100MHz. This is due to constraints such as power consumption, real-time operation, and bandwidth. Therefore, reconstruction of $\alpha(t)$ is not possible through dense frequency sampling, unless strong assumptions about $\alpha(t)$ are made. In this section we introduce a framework that uses data-driven priors to estimate $\alpha(t)$ from sparse frequency measurements.

A. Data-driven Frequency Estimation

The proposed framework is shown in Figure 1. First, we concatenate the measured brightness pairs $(b_{\omega_k,0}, b_{\omega_k,\frac{\pi}{2}})$. Brightness images with n_r rows, n_c columns, and K frequencies, will result in a $n_r \times n_c \times 2K$ tensor B . We define a frequency estimation network, g_θ , that interpolates/extrapolates the frequencies up to ω_S , where $\omega_S \geq \omega_k$:

$$g_\theta(B) = \{b_{\omega_1,0}, b_{\omega_1,\frac{\pi}{2}}, \dots, b_{\omega_S,0}, b_{\omega_S,\frac{\pi}{2}}\} \quad (5)$$

To avoid phase wrapping ambiguities B includes ω_1 .

Why should g_θ be able to learn this form of frequency super-resolution? We observe that, although, transient pixel waveforms can have arbitrary shapes, most waveforms have a low-dimensional underlying structure. For example, in scenarios where direct illumination is dominant, one frequency is sufficient to estimate the transient pixel, and hence, all of

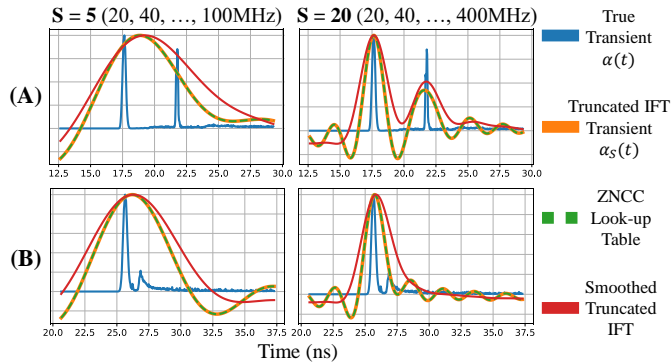


Fig. 3: Truncated IFT. Examples of transient pixels reconstructed using a truncated IFT. A truncated IFT transient, $\alpha_S(t)$, with frequencies up to 100MHz (1st column) is not able to separate sparse MPI peaks (Row A), and diffuse MPI (Row B) introduces a bias in the peak. Introducing higher frequencies in the truncated IFT (2nd column) allows $\alpha_S(t)$ to separate the sparse MPI, and the diffuse MPI peak bias becomes smaller.

its Fourier coefficients. For sparse MPI where there are two peaks (Row (A) in Figure 3), two frequencies are sufficient [33]. Finally, for diffuse MPI (Row (B) in Figure 3) the transient pixel can be approximated by a low-dimensional parametric model [38], which reduces the solution’s degrees of freedom. Based on this observation, we hypothesize and empirically demonstrate that the priors learned by g_θ enable it to interpolate/extrapolate frequencies from a few input frequencies.

B. The dToF Representation

One way to estimate $\alpha(t)$ from the output Fourier coefficients at $\omega_1, \dots, \omega_S$ is to compute its truncated Fourier Series with the first S terms:

$$\alpha_S(t) = \sum_{s=1}^S A_{\omega_s} e^{i(\omega_s t - \phi_{\omega_s})} \quad (6)$$

Equation 6 can be implemented by taking the Inverse Fourier Transform (IFT) of the estimated brightness pairs in Equation 5, with $(b_{\omega_s,0}, b_{\omega_s,\frac{\pi}{2}})$ as the real and imaginary parts of ω_s . A truncated IFT will contain Gibbs ringing artifacts as shown in Figure 3. These artifacts are not an issue if we only need the maximum peak. However, to find other peaks, it is useful to apply a smoothing function, like a Hamming window [46], that reduces the ringing but does not completely remove higher frequencies (red line in Figure 3). Moreover, besides a truncated IFT, other transient estimation methods like the ones discussed in Section II are applicable. We limit our analysis to the truncated IFT due to its simplicity, minimal assumptions, and relation to a robust depth decoding method discussed next.

Robust Depth Estimation: Given $\alpha_S(t)$, assuming diffuse reflections, depths are encoded by the maximum peak location, i.e., $\text{argmax } \alpha_S(t)$. In other words, $\alpha_S(t)$ is a depth lookup table. It turns out that $\alpha_S(t)$ has an interesting connection

to the lookup table used in the zero-mean normalized cross-correlation (ZNCC) depth decoding algorithm, originally proposed in the structured light context [13], [47], and recently applied to iToF [2]. In our case, the projected/reference signals are sinusoids at multiple frequencies, and the observed signals are the brightness measurements estimated in Equation 5. The ZNCC between the reference and observed signals results in the ZNCC depth lookup table (green line in Figure 3). We observe that the ZNCC lookup table is equivalent (up to a scale) to $\alpha_S(t)$ (orange line in Figure 3). Assuming a direct-only illumination model, ZNCC decoding is near-optimal in the presence of additive white Gaussian noise [13]. Therefore, given Equation 5 2S brightness measurements, we can use the max peak of the ZNCC lookup table or $\alpha_S(t)$ for noise-robust depth estimation. Interestingly, despite the direct-only assumption in ZNCC decoding, the lookup table will account for direct and indirect light paths, given enough frequencies. This means that, although, ZNCC’s optimality may not hold for pixels with MPI, it will still mitigate MPI.

Flexible Depth Estimation: In certain challenging depth sensing scenarios, like sparse MPI, the maximum peak may not encode depth. Examples of these scenarios include: specular MPI, optical cross-talk, and depth discontinuities. Some of these scenarios may not be modeled in the training set (e.g., optical cross-talk), or in the case of depth discontinuities the correct peak may be application-dependent (see supplement for an example), making them challenging to resolve using a data-driven model. Fortunately, the dToF response that arises in all of these situations follows a similar sparse 2-path model, which will be well-represented in the dataset at glossy surfaces (e.g., wood floor in Figure 4) and at edge pixels. Therefore, the data-driven model in iToF2dToF should be able to generalize and predict the correct sparse dToF response. Finally, we can design rule-based peak finding algorithms around the flexible dToF representation to recover the correct depths in these situations.

V. DATASETS AND IMPLEMENTATION

In this section, we introduce our simulator and new synthetic Multi-Frequency ToF (MF-ToF) dataset. We also describe the acquired real datasets. Lastly, we discuss the architecture used for iToF2dToF and the baseline models.

A. Simulator and Synthetic Datasets

We implemented a data generation pipeline and created the MF-ToF dataset. Table I outlines the aspects that our dataset improves over previous datasets [3], [6]–[8].

iToF Simulator: We render transient images using MitsubishiToF [43], [48]. The iToF simulator takes as input the transient images, sensor parameters, and frequency, to produce 4-phase sinusoid measurements. Assuming sinusoid functions works well in practice because commercial iToF modules come calibrated. Finally, read and photon noise are added, and we check for saturation. To validate the simulator’s signal and noise levels we use real iToF data to tune the simulator parameters (see supplement).

	FLAT [7]	DeepToF [6]	E2E ToF [3]	DA CNN [8]	MF-ToF (Ours)
Number of Unique 3D Scene Models	70	25	5	35	25
Scene Layout Realism	Low	High	High	High	High
Scene Textures Realism	Low	Low	Low	High	High
Non-Diffuse Materials	None	None	None	None	Plastic - described in Mitsuba [48]
Unique Camera Views per Scene	30	7	250	2	200
Total Images w/out Augmentation	2100	175	1250	70	5,000
Simulator Validation	Yes	No	No	No	Yes
Number of Frequencies	3	1	2	3	30

TABLE I: Synthetic iToF Dataset Comparison.

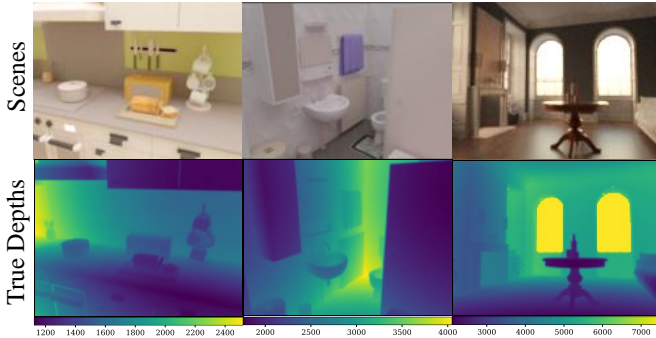


Fig. 4: Synthetic Scenes from the MF-ToF dataset.

3D Scenes and View Generation: We gathered 14 Mitsuba scene models from [49], and 11 Blender scene models from [50] which we convert to Mitsuba. The scenes have realistic layouts, textures/albedos, and diffuse and glossy materials as seen in Figure 4. For each scene, we semi-automatically generate 200 views used to render 5000 transient images.

MF-ToF Dataset: We simulate 5000 iToF images containing frequencies from 20MHz to 600MHz in steps of 20. To cover a wide range of SNR levels we simulate and average multiple frames. According to our simulator validation, averaging 2 frames has similar noise levels to an exposure time of 0.3ms in the real sensor. Therefore, for each image the number of averaged frames is randomized between 1 and 12 to emulate exposure times ranging from 0.15-1.8ms. We use this dataset for training. We simulate 4 more datasets with varying number of averaged frames to evaluate the performance of each model at different SNR levels (Figure 5). The dataset has a 120x160 spatial resolution.

For more details about the simulator and the synthetic datasets, please refer to the supplementary document.

B. Real Datasets

We use Sony’s IMX516 iToF module with 480x640 resolution for data collection. All images are resampled to 120x160 to match the MF-ToF dataset resolution. We can control the exposure time from 0.1ms up to 1ms. The IMX516 is configured and calibrated to take measurements at 20MHz and 100MHz by the manufacturer, and raw data access is available at these frequencies. Unfortunately, we are unable to

configure additional frequencies due to unavailability of low-level access. In addition to real-world scenes like the ones in Figures 1 and 9, we acquire scenes in controlled scenarios with ground truth depths. Namely,

- **Wall scenes:** We imaged a flat wall at 8 depths (0.25-2m in steps of 0.25m), at 3 exposures (0.15, 0.3, 0.5ms), and with 3 surface reflectances (5, 20, 50%). To verify the true depth, we fixate a cross-shaped laser distance sensor next to the iToF module. For alignment, we attached a mirror to the wall and made sure that the reflected laser pointer returned to the emitting point, ensuring that the sensor and wall plane were parallel.
- **MPI scenes w/ ground truth:** We captured 7 real-world scenes with partial ground truth. Figure 7 shows 2 of them. To obtain ground truth depths we average 100 frames of an empty scene with negligible MPI (e.g., a wall or an empty table as in Figure 7). We use the noise-free data to compute ground truth depths with the Phasor method described in Section VI-A. Afterwards, we capture the same scene a second time with objects placed in it. We manually create a mask indicating the regions where ground truth depths can be obtained from the first capture (see Figure 7). Each scene was captured at 4 exposures (1, 0.5, 0.2, 0.1ms), to cover a wide range of SNR levels.

C. Training and Implementation

The inputs to the network are frequency measurements at 20 and 100MHz, where each frequency has 2 input channels ($b_{\omega,0}, b_{\omega,\frac{\pi}{2}}$). In the iToF2dToF models the network outputs the interpolated and extrapolated frequencies up to a given maximum frequency. We normalize each frequency by dividing by its amplitude [3]. Although, we find that using amplitude information improves the performance of all models, we also observe that models trained with amplitude information do not generalize well to real data. This is due to the lack of calibration of the amplitude in commercial iToF modules (only phase is calibrated). Extensive calibration [7] or more complex architectures [8] may help solve this problem. Nonetheless, the benefits of iToF2dToF hold with or without amplitude information (see supplement).

The network architecture used for all iToF2dToF and baseline models was a U-net [51] with skip connections, ReLU activations, and learned upsampling, implemented in PyTorch [52]. The number of model parameters ranges between 1.873-1.877M depending on the number of output channels. We minimize the L1 loss between the U-net’s output and the target output. For a detailed description of the U-net architecture, please refer to the supplement.

For training we split the dataset into train, valid, and test sets. The training set is composed of all views generated from 21 scenes (4200 instances). The validation and testing sets are each composed of views generated from 2 scenes. Unless stated otherwise, we train all models using the ADAM optimizer [53] with a constant learning rate of 0.0001 for 300 epochs, followed by 700 epochs with a linearly decaying learning rate. We use a batch size of 32. During training, we mask pixels with depths greater than 7.5m (max depth for

Model	Synthetic Test Set Percentile MAE (mm)			
	0-75%	75-85%	85-95%	95-99%
Phasor (No Noise) [1]	9.53	29.58	46.37	94.79
SRA (No Noise) [37]	13.97	41.75	62.70	126.51
Depth2Depth [6]	13.40	42.21	69.07	136.96
iToF2iTof Baseline	10.56	31.93	49.71	101.82
iToF2Depth [3]	7.49	21.86	34.99	88.03
iToF2dTof @ 140MHz	9.23	28.08	44.31	91.53
iToF2dTof @ 200MHz	7.85	23.26	36.69	78.60
iToF2dTof @ 300MHz	7.41	21.23	33.33	74.68
iToF2dTof @ 400MHz	7.19	20.42	32.18	71.56
iToF2dTof @ 500MHz	7.22	20.40	32.17	72.12
iToF2dTof @ 600MHz	7.33	20.66	32.76	76.13

TABLE II: Percentile MAE calculated on the simulated test set containing a wide range of SNR levels. Training iToF2dTof to extrapolate to higher frequencies improves performance up to around 400MHz.

20MHz) and with “infinite” depths corresponding to pixels looking at empty space (e.g., open windows or doors). During testing we remove images that contain these invalid pixels. Furthermore, during training, we apply random flips for data augmentation. At each epoch we evaluate the model’s loss on the validation set and we keep track of the model with the lowest validation loss.

VI. EXPERIMENTS AND RESULTS

In this section, we perform an ablation study to find the maximum frequency iToF2dTof can effectively extrapolate to, and compare it to multiple traditional and data-driven iTof models. The synthetic test set has 200 instances. We evaluate the robustness to noise on real and synthetic data. Finally, we demonstrate the flexibility of iToF2dTof on two real examples of specular MPI and optical cross-talk.

Performance Metric: To quantify performance we use percentile mean absolute errors (MAE), similar to [3], [21]. For each image, the depth errors are sorted from lowest to highest, divided into 4 percentile groups (0-75%, 75-85%, 85-95%, 95-99%), and the MAE is calculated within each group. This grouping allows to understand the performance in high SNR/low MPI (i.e., 0-75% percentile) and in low SNR/high MPI (i.e., 85-99% percentile) regions. When calculating the percentile MAE on synthetic data, we mask edge pixels with depth discontinuities (i.e., flying pixels) because the ground truth depth is not reliable. We do not consider pixels with the largest 1% error to avoid invalid pixels that arise from unmasked flying pixels, or infinite ray pixels (may occur at the intersection of two meshes).

A. Baseline Comparison and Ablation Study

We evaluate iToF2dTof with different maximum frequencies and compare it against the following approaches:

- **Phasor:** Depths are computed using a lookup table approach often used for multi-frequency iTof [1], [2].
- **SRA:** Depths are computed using the sparse reflections analysis technique introduced in [37].

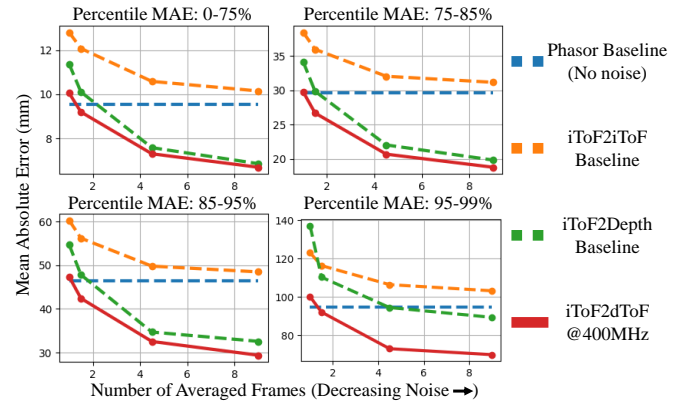


Fig. 5: **Noise vs. Errors.** We simulate the same test set at varying SNR levels as described in Section V-A. Each model was trained with images containing the full range of SNR levels. The Phasor baseline does not contain noise and is only shown to confirm the MPI correction capabilities of the data-driven models.

- **Depth2Depth:** A network trained to remove noise and MPI errors from the depths produced by Phasor. This is a similar model to [6], without the pre-training stage.
- **iToF2Depth:** A network trained to map noisy iTof data to denoised and MPI-free depths. This is a similar model to [3], but with a smaller network. This model required more training to converge, so instead of 700 epochs of linearly decaying learning rate, we use 1700.
- **iToF2iTof Baseline:** A network trained to denoise the input iTof measurements.

Table II compares the performance of iToF2dTof and the aforementioned baselines. All the data-driven models use the U-net architecture described in Section V-C. Performance of iToF2dTof improves as we increase the maximum frequency it extrapolates to. Around 400MHz performance plateaus, and further extrapolation does not lead to better results. For the remainder of the paper the iToF2dTof model extrapolates up to 400MHz. Please refer to the supplement for additional results showcasing the effect of frequency on depth errors and also the recovered transient signals.

Most data-driven approaches are able to correct for MPI to some degree, as seen in Table II. This is evident by comparing their metrics with Phasor, whose depth errors are solely due to MPI because we do not add noise to it. Additionally, we observe poor performance by the SRA model. This is likely due to SRA’s K-path modeling assumption not being true for scenes without reflective objects, and also only providing 2 frequencies. Similar to [3], we find that Depth2Depth with a U-net architecture performs worse than a U-net that uses the raw measurements as input (i.e., iToF2Depth). Overall, iToF2dTof outperforms all the evaluated models. Other MPI correction methods [14], [30], [33], [35], [36], [38] require special acquisition strategies or more frequencies, making them difficult to compare with.

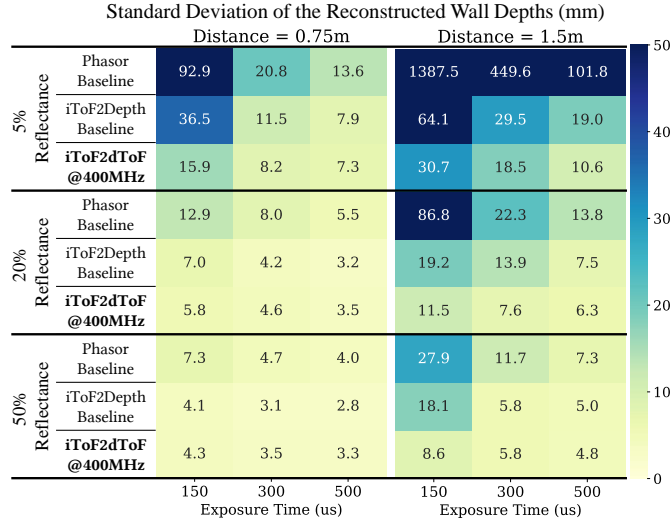


Fig. 6: Wall Depths Standard Deviation. As described in Section V-B, we image a wall at different distances, under 9 combinations of exposure and reflectance settings. The reconstructed depths by iToF2dToF exhibit the lowest standard deviation at most SNR levels, particularly at low SNR.

B. Robustness of iToF2dToF

In this section, we demonstrate the performance of iToF2dToF in scenarios with a wide range of SNR levels.

Robustness on Synthetic Data: Figure 5 shows performance at different SNR levels. As we decrease the test set SNR, the performance gap of iToF2dToF and the end-to-end model (iToF2Depth) increases. Surprisingly, in the lowest SNR setting iToF2Depth performs worse or comparably to a denoising network (iToF2iTof). We find that using a larger network for iToF2Depth, helps improve its robustness to noise. Nonetheless, as shown in the supplement, the larger network continues to perform worse than iToF2dToF.

Robustness in Real Wall Dataset: Figure 6 shows standard deviation of the reconstructed depths for a planar wall at different SNR levels. We apply light gaussian smoothing on the raw data for Phasor. At low SNR settings iToF2dToF achieves $\sim 2x$ lower standard deviation. In the supplement we show results with a similar trend at more distances.

Robustness in Real-world Data: Table III summarizes the percentile MAE obtained from 28 scenes (7 scenes, 4 exposures per scene) with partial ground truth, as described in Section V-B. Figure 7 shows the depth errors for 2 of them. Quantitatively, iToF2dToF achieves lower percentile MAE than all baselines, and outperforms iToF2Depth in 6 out of 7 scenes. Qualitatively, Figure 8 shows that iToF2dToF recovers depth images with fewer artifacts. In the supplement, we present extensions of Figures 7 and 8 for all acquired scenes and additional qualitative results.

C. Flexibility of iToF2dToF

We integrate iToF2dToF with two rule-based algorithms to resolve specular MPI and optical cross-talk. In the supplement we show two more examples that use the flexible dToF representation for specular MPI and depth refinement.

Real-world Test Set Percentile MAE (mm)				
Model	0-75%	75-85%	85-95%	95-100%
Phasor [1]	42.51	234.93	440.18	1150.66
iToF2iTof Baseline	10.12	32.58	43.21	68.31
iToF2Depth [3]	7.70	21.82	30.46	65.05
iToF2dToF @400MHz	6.64	19.46	27.57	60.29

TABLE III: Percentile MAE for real-world scenes with ground truth captured as in Figure 7.

Specular MPI: The maximum peak of specular pixels may not encode the true depth because the direct reflection (1st peak) is not the maximum, e.g., TV pixel in Figure 1. In Figure 1, we adapt iToF2dToF to use a 1st peak finding algorithm. First, we find candidate peaks with Scipy’s [54] built-in *find_peaks* function. The largest 2 peaks, whose heights are at least 2x the median of the transient pixel, are selected. Finally, the 1st peak is selected and a 3x3 median filter is applied to remove outliers caused by noisy peaks.

Optical Cross-Talk: When a scene contains high contrast regions, such as a bright foreground and dark background, the signal from the bright foreground pixels leaks into the dark regions. This ToF artifact is a type of MPI attributed to lens inter-reflections [55] and often called optical cross-talk. Fundamentally, cross-talk is a kind of sparse MPI where the correct depth corresponds to the second peak in the transient response. Despite not explicitly modeling optical cross-talk in the training set, in Figure 9 we show how iToF2dToF can be integrated with the following peak finding algorithm to resolve cross-talk.

We begin by finding high contrast regions in the amplitude image. To this end, we take the absolute difference between the amplitude image and a blurred amplitude image, and divide by the amplitude image. We threshold this ratio to obtain a mask of high contrast regions. This high contrast mask is then multiplied with a second mask indicating all pixels with a 2nd peak. To find the 2nd peak we use the same algorithm as for specular MPI. Finally, we use the mask to select the pixels that should use the depth of the second peak. This algorithm leads to a few outliers in the 2nd peak depth image, so a median filter is applied.

VII. DISCUSSION AND LIMITATIONS

Data-driven iToF models that perform supervision on the final depthmap representation can achieve good performance as long as the training dataset provides explicit supervision for each scenario. In practice, a large, diverse, and accurate dataset is challenging to collect or even simulate. To alleviate this depthmap supervision dependency, we propose to learn an intermediate representation that encodes depths, but decouples the depth estimation step from training. At test time, depths are estimated from the intermediate representation using rule-based algorithms that embed domain knowledge, enabling high-performance in multiple challenging scenarios.

More broadly, end-to-end learning-based models that perform supervision on the final target representation (e.g., depthmaps in our case) have achieved state-of-the-art in many applications. Our work suggests that it is sometimes beneficial

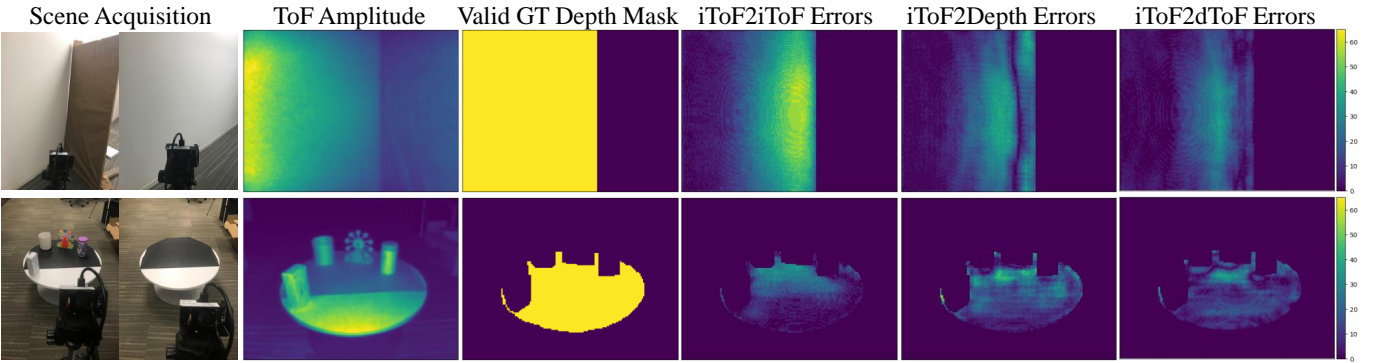


Fig. 7: Real-world MPI Correction. To quantitatively evaluate the MPI correction capabilities of each method, we acquire scene pairs as shown in the left-most images. We capture the scene with and without objects in it, and use the depths from the scene without objects as the ground truth depths. We manually draw masks that indicate regions where ground truth depths are known. In both scenes, captured with a 1ms exposure time, iToF2dTof achieves the lowest depth errors.

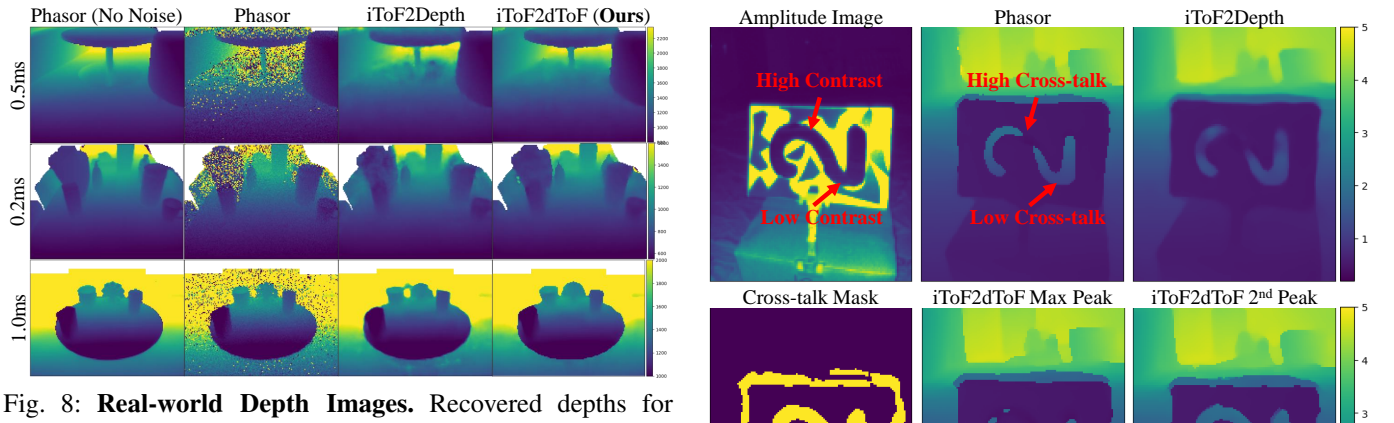


Fig. 8: Real-world Depth Images. Recovered depths for multiple scenes at various exposure times. The Phasor (No Noise) images provide an approximate view of how the correct depth image should look like. For visualization purposes, we mask pixels (white regions) that exhibit phase wrapping or that were still noisy in the “noiseless” Phasor image. We find that iToF2dTof generates higher-quality depth maps, particularly, in low SNR regions.

to perform supervision on a sensible intermediate representation, from which the final representation can be extracted using rule-based algorithms. This approach was particularly useful in corner cases and ambiguous scenarios where it was easier to perform supervision on the intermediate representation. Finally, in the more common scenarios, the proposed method also achieved good performance, in particular, at low SNR.

Scattering Media: In the supplement we analyze the generalization of iToF2dTof to scattering media. Although, iToF2dTof does not completely break like other learning-based models, our per-pixel transient analysis suggests poor generalization to this scenario.

Other Architectures: To isolate the benefits of iToF2dTof’s “Input2Output” representation comparisons were done with networks of similar size, same architecture, and same training set. Specifically, we chose a fixed U-net architecture, and trained it on different representations. An extended analysis on how other architectures (e.g., KPN [7], [9]) work with all representations is an interesting avenue for future work.

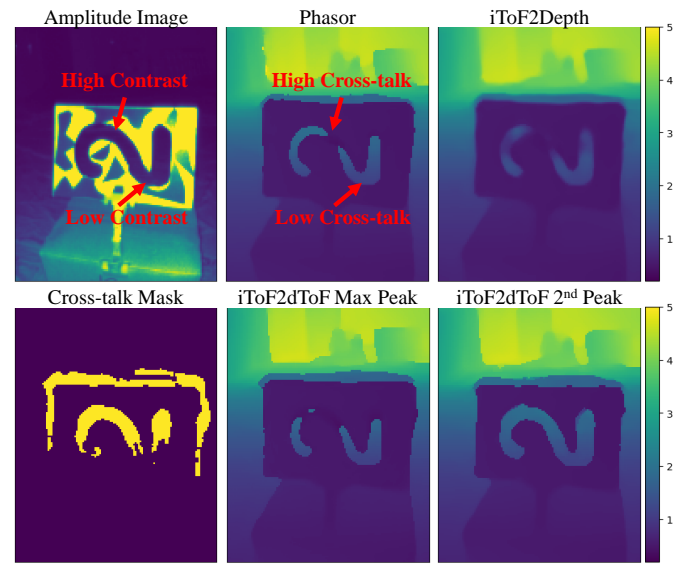


Fig. 9: Optical Cross-Talk Correction. Cross-talk arises in ToF images with *high contrast* regions. In these regions all methods incorrectly assign the foreground depth to background pixels. Fortunately, the dToF representation and the amplitude image allow us to identify high contrast regions and correct those pixels by selecting the depth of the second peak (iToF2dTof 2nd Peak).

Bridging the iToF and dToF Gap: dToF sensors overcome the challenges iToF faces by directly capturing transient images. However, their low-resolution, high-cost, moving parts, and high power consumption, prevent their use in certain applications. To some degree, we are closing the gap between iToF and dToF by exploring the extreme transient imaging case where only *two* frequencies are available. We can indeed reconstruct the transient from the limited input, albeit, at a lower time resolution than current dToF sensors. An interesting direction for future work could explore the limits of data-driven iToF-based transient imaging with additional and higher frequencies [56] and its applications [57].

Acknowledgements: The authors would like to thank Jiaojiao Tian, Yu Yao, and Yin Zhang from Tetras AI for their help on the data collection.

Supplementary Document for “iTof2dToF: A Robust and Flexible Representation for Data-Driven ToF Imaging”

S. 1. SIMULATOR AND SIGNAL LEVEL VALIDATION

To simulate realistic signal and noise levels, we tune the exposure and power parameters of our simulator by comparing the simulated images with similar real captured images. The real and synthetic ToF images have the following parameters:

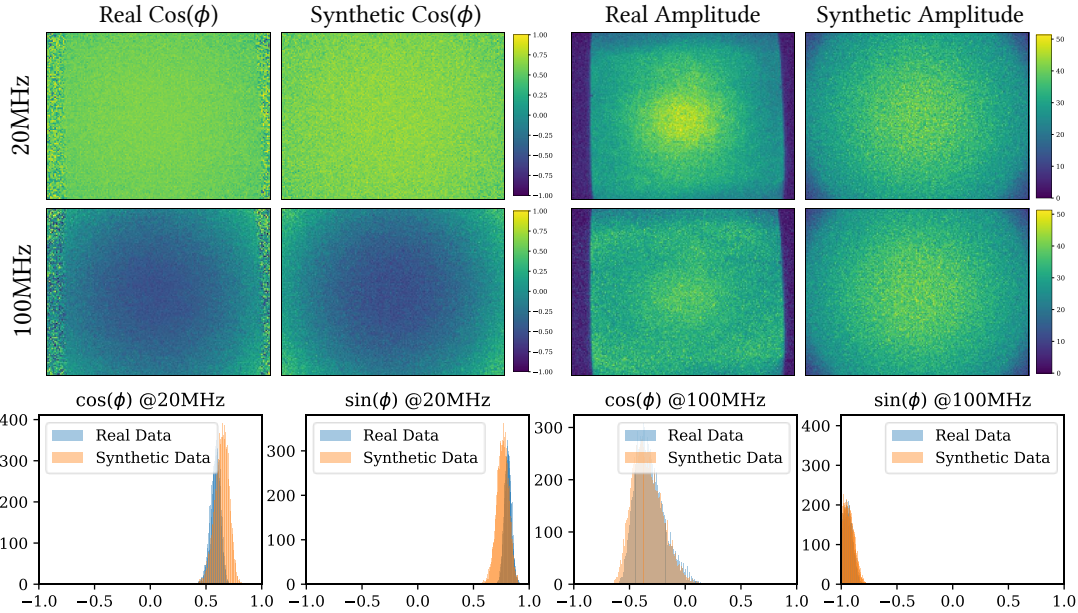
- **Real Data Parameters:** We captured dual-frequency ToF data of a white flat plain 500mm, 1000mm, and 2000mm away from the camera. The images are captured using a 0.3ms exposure and a light source average power of 1W. For each frequency, dual-tap 4-phase measurements are made, resulting in 8 measurements per frequency.
- **Simulated Data Parameters:** We simulated dual-frequency ToF data of a white flat wall 500mm, 1000mm, and 2000mm away from the camera. The exposure time is also set to 0.3ms, and 4-phase measurements are simulated per frequency. To match real data acquisition 2 frames are averaged for each phase. To approximately match the signal levels (i.e., amplitude) of the real ToF data we set the average source power in the simulation to 32W.

To obtain $(b_{\omega,0}, b_{\omega,\frac{\pi}{2}})$ from 4-phase data we simply take the difference between the 0-180 and 90-270 measurements.

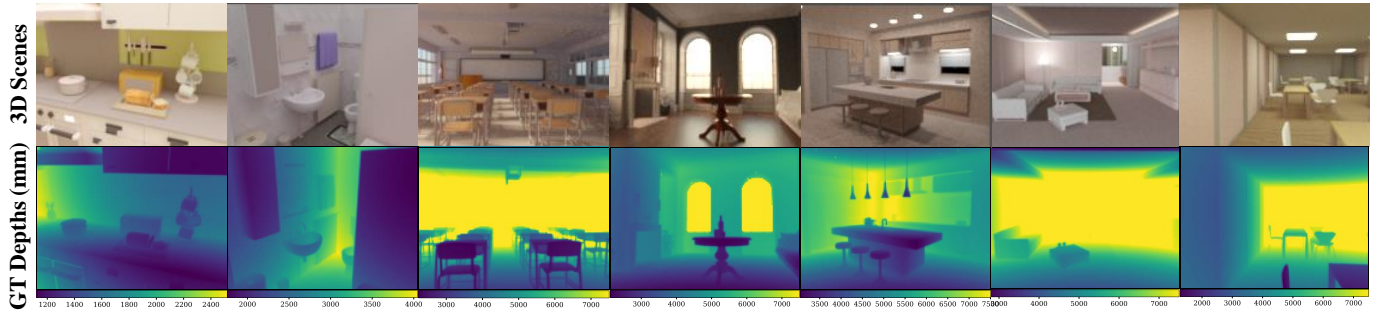
Amplitude Images: Figures 1 and 17 compare the synthetic and real data with the above parameters. Due to the limited bandwidth of the real ToF camera, the 100MHz amplitude image is lower than the 20MHz. To compensate for bandwidth in our simulation, we tuned the simulation power parameter such that the amplitude images at 20MHz and 100MHz fall in between the real amplitude images. This leads to similar noise levels, as shown in the histograms of the recovered phases.

Phase Images: Qualitatively, the recovered phase images match for the captured and simulated scenes, as shown in Figures 1 and 17. Quantitatively, the histogram of phases for the captured and simulated data matched for 100MHz. For 20MHz, synthetic data displays higher variance in the histogram, which is expected since the simulated signal levels are lower. Furthermore, due to imperfect calibration at 20MHz, we observe a small phase offset between the real and synthetic data. Unfortunately, due to the lack of low-level control of the ToF module we are not able to correct for this. Nonetheless, our results show that this small phase offset does not have a significant effect on the performance of the trained models.

Real vs. Synthetic Data of a Flat Wall 1000mm Away



Supplementary Figure 1: **Synthetic vs. Real ToF Images** of a flat wall 1000mm away from the camera. The first row shows the real and synthetic phase images (columns 1 and 2), and the real and synthetic amplitude images (columns 3 and 4), for 20MHz. The second row shows the same images for 100MHz. The flat plain that was captured did not cover the full field of view of the camera, as seen in the real phase and amplitude images. Therefore, when calculating the distribution of the recovered phases (third row), we cropped the real and synthetic images such that we only included the valid pixels.



Supplementary Figure 2: **Dataset Overview.** Example synthetic 3D scenes from the dataset.

S. 2. IMPLEMENTATION DETAILS

A. Transient Data Generation and iToF Simulator

In this section we describe the synthetic data generation pipeline we used to create the MF-ToF dataset used for training and the ablation studies. Our pipeline shares some similarities to the data generation pipelines developed for previous data-driven iToF works [3], [6]–[9], and some differences which we will point out.

Transient Data: For transient rendering we use MitsubaToF [43], an extension to the widely used Mitsuba renderer [48]. Previous works have used a modified pbrt-v3 [58] for time-resolved rendering [3], [9], proprietary software [8], or recent transient rendering software [6], [7], [41]. We chose Mitsuba because it is faster than pbrt-v3 [59], and it provided a plugin to convert Blender 3D scene models to Mitsuba [60]. Using Mitsuba’s notation, we use a pulsed *spot* light emitter, with a 30 degree *beamwidth*, that flash-illuminates the scene for transient rendering. These parameters match the simulated and real sensor’s FoV. All transient images in this paper have a 50ps time resolution and 2000 time bins resulting in a time domain of 0-1000ns. This time domain contains all light paths that are 0-20 meters in length, and provides a depth resolution of 5mm.

3D Scene Models: We gathered 14 Mitsuba scene models from this repository [49]. Additionally, we downloaded 11 Blender scenes from [50] and converted them to Mitsuba using the exporter plugin [60] along with our post-processing scripts to correct for some errors made by the plugin. For all scenes we change completely transparent and completely specular (mirror-like) materials to diffuse materials with a constant randomly chosen albedo. This avoids over-fitting to these corner cases, for which even an ideal dToF system cannot recover depths because fully transparent and specular materials will not have a direct illumination signal. Our 3D scene models, as shown in Figure 2, contain realistic texture/albedos and also diffuse and glossy materials (smooth plastic in Mitsuba terminology). For simulating textures/albedos, previous works have relied on randomizing constant albedos over the full scene model [3], [6] or multiplying the resulting rendered images by a texture image [7], which leads to less realistic transient images.

Camera View Generation: For a given 3D scene model we semi-automatically generate 200 camera views. To guarantee a diverse set of camera views, we manually pick 4-10 view points for each scene. We use the manually picked view points as the starting point for our automatic camera trajectory generation. When automatically generating a new camera view we take a small step forward in the current view direction, and then apply a small random rotation to the current view direction. We check for collisions by generating the depth map of the current view and checking if any points are closer than 200mm. If a collision is detected the camera view direction is flipped. If we detect the camera moving towards empty space we slowly rotate the camera until it is looking toward scene content again. Our camera view generation program relied heavily on Mitsuba’s Python API. To create large synthetic ToF datasets, previous works, have also generated camera views automatically [3] and manually [6], [8].

iToF Simulation: The input to our iToF simulator is a transient image. The transient image is convolved with a sinusoidal light source modulation function, and the resulting function is the signal arriving at the sensor. Similar to previous works [3], [6], [9], we find that we obtain good generalization assuming sinusoidal signals because the real iToF module functions are calibrated. In other words, the iToF module’s output phase measurements are roughly the same as an ideal sinusoid phase measurements. The arriving signal is multiplied with the sensor demodulation function, and integrated. Similar to previous works, we do not consider ambient illumination² [3], [7]. Next, the integrated signal is scaled according to different sensor parameters (quantum efficiency, exposure time, electron to voltage factor) obtained from the iToF module used in experiments. Finally, read and photon noise are added to the iToF measurement. To achieve realistic signal and noise levels we calibrate the average light source power parameter used in simulation with real iToF data (details in Section S. 1).

²In practice, iToF modules operate indoors where ambient illumination is low, and are also equipped with spectral filters which largely mitigate the ambient illumination incident on the sensor.

B. Synthetic Multi-Frequency ToF (MF-ToF) Dataset

Using the simulator and the 5000 transient images, we generate the synthetic MF-ToF dataset. Different from previous works, we simulate multiple frequencies from 20MHz to 600MHz in steps of 20. A 20MHz repetition frequency leads to an unambiguous depth range of 7.5m, which is sufficient for indoor applications. To cover a wide range of SNR levels we simulate multiple frames and average them. According to our simulator validation in Section S. 1, averaging 2 frames leads to similar noise levels as using an exposure time of 0.3ms in the real sensor. Therefore, for each image the number of averaged frames is randomly chosen between 1 and 12 to emulate exposure times ranging between 0.15-1.8ms, which are reasonable in commercial iToF cameras [5]. We use this dataset for training. Furthermore, we simulate 4 additional datasets where the range of averaged frames is 1-1, 1-2, 3-6, 6-12 (instead of 1-12), and we use these datasets for evaluating the performance of each model at different SNR levels as shown in Section 6.2 in the main document.

Limited by the transient rendering time (\sim 7 days on a 32 core machine), the dataset has a 120x160 spatial resolution. Although, the dataset has a lower spatial resolution than current commercial iToF sensors, a higher resolution dataset may not be essential to learn to correct MPI. This is because MPI is often similar for large regions in the image, therefore, it is an artifact that can be resolved at a lower resolution. Nonetheless, the denoising component of the model will benefit from a high-resolution synthetic dataset. Therefore, future iterations of the MF-ToF dataset will be at the full resolution of commercial iToF sensors.

Network Architectures								
Name	InConv	D1	D2	U1	Conv1	U2	Conv2	OutConv
Layer	Conv2D + ReLU + Conv2D + ReLU	Conv2D + ReLU + Conv2D + ReLU	Conv2D + ReLU + Conv2D + ReLU	ConvTranspose2D	Conv2D + ReLU + Conv2D + ReLU	ConvTranspose2D	Conv2D + ReLU + Conv2D + ReLU	Conv2D
	7x7 / 3x3	3x3 / 3x3	3x3 / 3x3		2x2		2x2	3x3 / 3x3
	1 / 1	2 / 1	2 / 1		2		2	1 / 1
Skip Connection	—	—	—	—	From D1	—	From InConv	—
Input	Raw ToF	InConv	D1	D2	[U1, D1]	Conv1	[U2, InConv]	Conv2
Channels I/O	4 / 64	64 / 128	128 / 256	256 / 128	256 / 128	128 / 64	128 / 64	64 / N _{out}
iToF2Depth Output - N _{out} = 1	64 x H x W	128 x $\frac{H}{2}$ x $\frac{W}{2}$	256x $\frac{H}{4}$ x $\frac{W}{4}$	128 x $\frac{H}{2}$ x $\frac{W}{2}$	128 x $\frac{H}{2}$ x $\frac{W}{2}$	64 x H x W	64 x H x W	1 x H x W
iToF2iTof Output - N _{out} = 4	64 x H x W	128 x $\frac{H}{2}$ x $\frac{W}{2}$	256x $\frac{H}{4}$ x $\frac{W}{4}$	128 x $\frac{H}{2}$ x $\frac{W}{2}$	128 x $\frac{H}{2}$ x $\frac{W}{2}$	64 x H x W	64 x H x W	4 x H x W
iToF2dTof Output - N _{out} = 2S	64 x H x W	128 x $\frac{H}{2}$ x $\frac{W}{2}$	256x $\frac{H}{4}$ x $\frac{W}{4}$	128 x $\frac{H}{2}$ x $\frac{W}{2}$	128 x $\frac{H}{2}$ x $\frac{W}{2}$	64 x H x W	64 x H x W	2S x H x W

TABLE IV: Detailed U-net network architectures. All models used the same backbone U-net. The only difference across models was the number of output channels in the *OutConv* layer. For iToF2Depth, the number of output channels was 1 ($N_{\text{out}} = 1$) because we directly output the depth image. For iToF2iTof, $N_{\text{out}} = 4$ because we output the denoised input ToF images. For iToF2dTof, the N_{out} depends on the maximum frequency we extrapolate, specified by the parameter S . In our main results we used a repetition frequency of 20MHz, and the maximum frequency we extrapolated to was 400MHz, making $S = 20$.

C. Network Architectures and Training

Input and Output: The inputs to the network are the raw dual-frequency iTof images at 20 and 100MHz. For each frequency, a raw measurement corresponds to 2 input channels ($b_{\omega,0}, b_{\omega,\frac{\pi}{2}}$). In the iToF2dTof models the network outputs the interpolated and extrapolated frequencies up to a given maximum frequency. We normalize each frequency by dividing by its amplitude [3], i.e., $\hat{b}_{\omega,0} = b_{\omega,0} / \sqrt{b_{\omega,0}^2 + b_{\omega,\frac{\pi}{2}}^2}$. As discussed in Section S. 6-B, we find that using amplitude information is useful, however, we also observe that models trained with amplitude information do not generalize well to real data.

Architecture: As outlined in Table IV we use a simple U-net [51] for all data-driven models in this paper. The U-net used skip connection (concatenated), ReLU activations, and learned upsampling. For downsampling and upsampling we used PyTorch's [52] built-in *Conv2d* and *ConvTranspose2d* with strides of 2. Depending on the number of output channels the total number of parameters in the models ranged between 1.873-1.877M.

Loss: We minimize the mean absolute error (i.e. L1 loss) between the U-net's output ($g_{\theta}(\mathbf{B})$) and the target output \mathbf{T} :

$$\mathcal{L}_{L1} = \frac{1}{N} \sum_i |g_{\theta}(\mathbf{B})_i - \mathbf{T}_i| \quad (7)$$

For iToF2Depth \mathbf{T} is the ground truth depth image, and for iToF2dTof \mathbf{T} will be the ground truth brightness images for $\omega_1, \omega_2, \dots, \omega_S$. We experimented with a more end-to-end training strategy where the loss function was the KL-Divergence of the recovered transient and the target transient. However, this approach performed comparably to a simple L1 loss on the output frequencies. Nonetheless, loss functions designed for data-driven transient imaging is a promising avenue for future work. While we acknowledge that advanced network design and training strategies explored in previous works [3], [6], [9], such as adversarial loss and pre-training, can further improve the performance, we focus on the benefits of the dToF representation because they are orthogonal to the benefits from such methods.

Training: For training we split the dataset into train, valid, and test sets. The training set is composed of all views generated from 21 scenes (4200 instances). The validation and testing sets are each composed of views generated from 2 scenes. We train all models in this paper using the ADAM optimizer [53] with a constant learning rate of 0.0001 for 300 epochs, followed by 700 epochs with a linearly decaying learning rate. IToF2Depth required additional training for convergence so we had to use 1700 epochs of linearly decaying learning rate. We use a batch size of 32. During training, we mask pixels with depths greater than 7.5m (max depth for 20MHz) and with “infinite” depths corresponding to pixels looking at empty space (e.g., open windows or doors). Furthermore, during training, we apply random flips for data augmentation. At each epoch we evaluate the model's loss on the validation set and we keep track of the model with the lowest validation loss.

S. 3. REAL WALL DEPTH RECONSTRUCTION STATISTICS

In this section we present additional real data results illustrating the robustness of iTof2dToF to noise. To this end, we compared the standard deviation and the histograms of the reconstructed depths of planar wall images at combinations of 8 distances (250mm-2000mm in steps of 250mm), 3 exposure times (0.5ms, 0.3ms, 0.15ms), and 3 reflectivities (50%, 20%, 5%). Figures 1 and 17 show the amplitude and phase images of the planar target we imaged at 3 of the 8 distances.

Data Acquisition Procedure: To verify the true depth for each planar wall target, we fixate a cross-shaped laser distance sensor next to the iTof module. For alignment, we attached a mirror to the target and made sure that the reflected laser pointer returned to the emitting point. In this way, we made sure the iTof sensor plane was parallel to the wall.

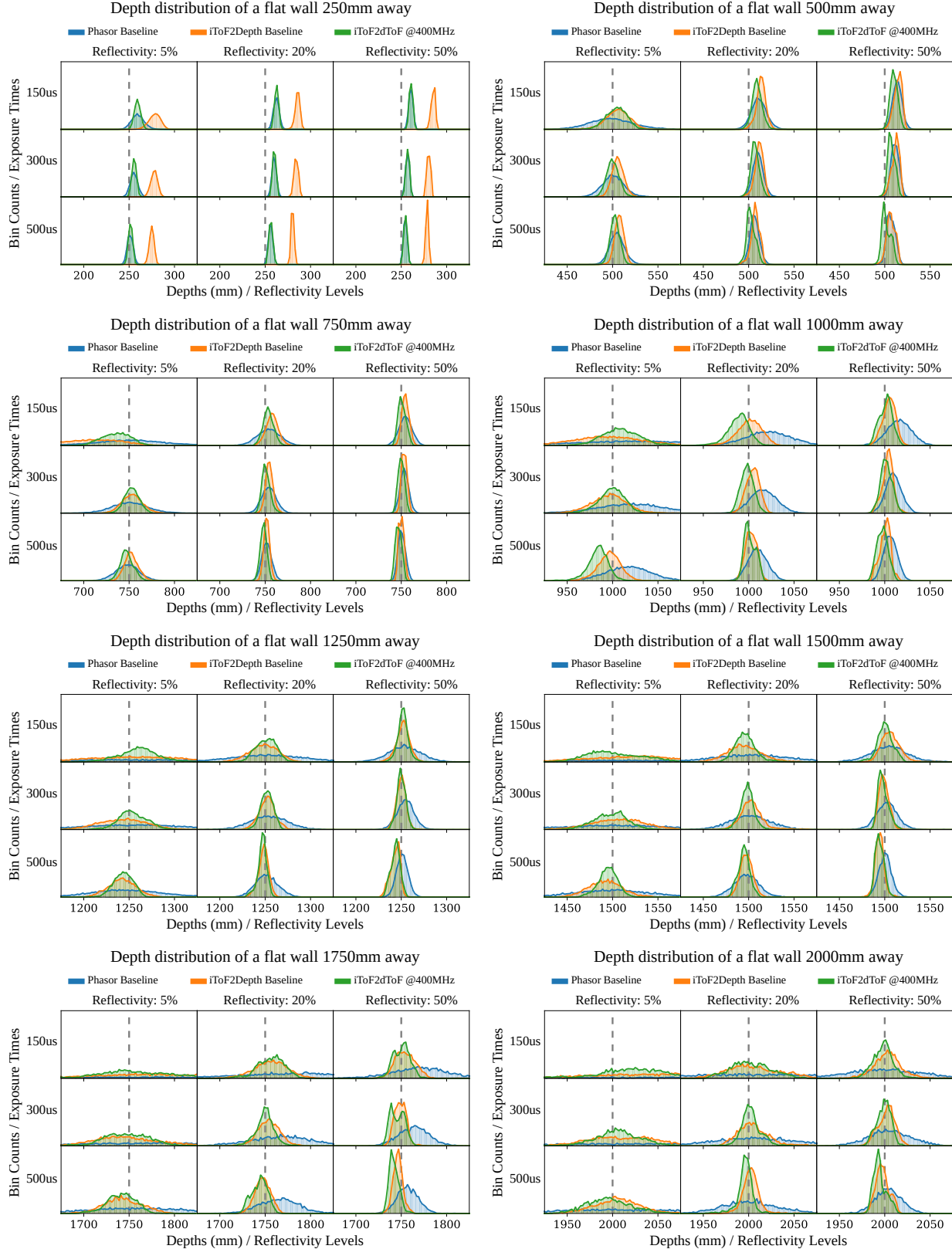
Main Observations: Figure 3 shows a quantitative comparison of the standard deviation of the reconstructed wall depths. For most SNR settings, iTof2dToF recovers depths with lower standard deviation than all methods. The benefits of iTof2dToF are most significant at low SNR settings (i.e., low reflectance and exposure). At the distance of 1.75m, for the lowest SNR setting, iTof2dToF has a higher standard deviation due to outliers in the recovered depths. Figure 4 shows the histograms of the recovered depths for 8 distances. We can observe that the distribution of recovered depths by iTof2dToF has lower variance at low SNR. Note that, due to sensor non-linearities and imperfect calibration, all methods exhibit a small depth bias that oscillates +/- 2cm around the ground truth depth, depending on the exposure and reflectivity settings. It is important to note that the histograms in Figure 4 do not include outliers, while the computation of standard deviations for Figure 3 does include outliers.

- **Artifacts on Depth Histograms:** The depth histograms for farther away depths (1750mm and 2000mm) are noisy. This is due to two reasons. As observed in Figures 1 and 17 the planar target we imaged covered a smaller portion of the sensors field of view as it was moved farther away. This means that fewer pixels were used when calculating the standard deviations and depth histograms. Furthermore, more outliers appear at the lowest SNR settings leaving even less pixels available to construct the histograms in Figure 4. For some combination of depth, exposure time, and reflectivity iTof2dToF has a distribution with 2 peaks centered at the ground truth depth. This might be due to a combination of the limited number of samples in the noisier histograms, and also the depth discretization of 0.5cm of the recovered transient pixel used for depth estimation.

Summary: Overall, in this simplified imaging scenario that only requires denoising to resolve depth errors, iTof2dToF consistently displays better robustness to noise than the evaluated baselines. Furthermore, despite the small depth bias observed in all models, the absolute depth accuracy on real data of the data-driven models (trained on synthetic data) appears to be comparable to a traditional method.



Supplementary Figure 3: Wall Depths Standard Deviation. We collect a iToF data of a wall at different distances, under 9 SNR settings obtained from the combination of different exposure times and reflectance. For most SNR levels, iToF2dToF achieves lower standard deviation in the recovered depths. The benefits of iToF2dToF are most significant at low SNR.

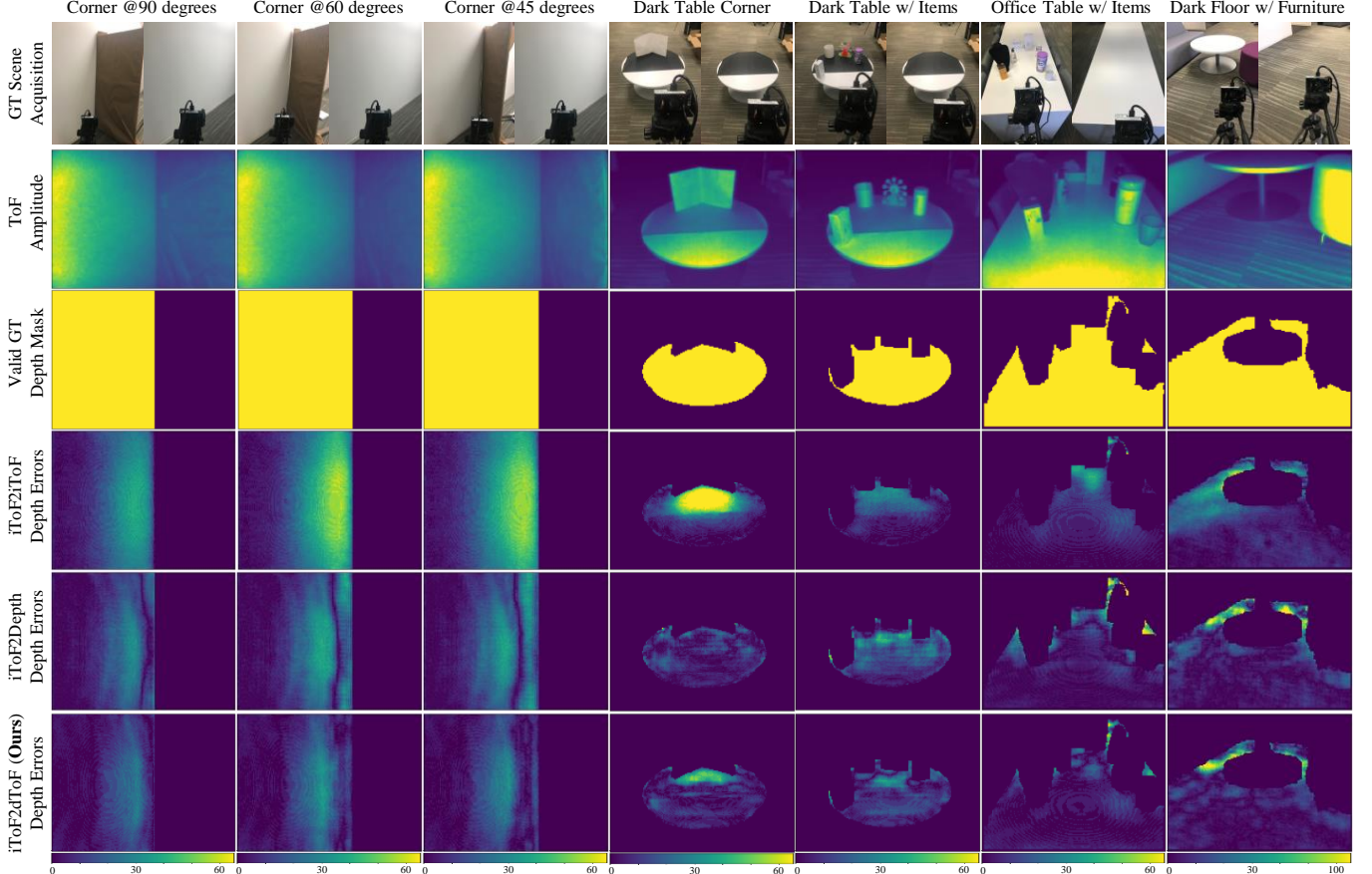


Supplementary Figure 4: Wall Depths Histograms. The variance of the estimated iToF2dToF depths is consistently lower than the baselines. Due to sensor non-linearities and imperfect calibration all methods exhibit a small depth bias that oscillates roughly +/- 2cm around the ground truth depth, depending on the exposure and reflectivity settings.

S. 4. REAL-WORLD EXPERIMENTS WITH GROUND TRUTH

In this section we present the results for the real-world test dataset with partial ground truth depths that we collected. The dataset contains 28 instances that come from 7 scenes captured at 4 exposure times ((1, 0.5, 0.2, 0.1ms)).

Ground Truth Acquisition Procedure: To obtain ground truth depths we captured and average 100 frames of an empty scene with negligible MPI (e.g., a wall or an empty table as shown in the first row of Figure 5). We use the noise-free dual-frequency data to compute ground truth depths using the Phasor method described in the main document in Section 6.1. Afterwards, we capture the same scene a second time, but with objects placed in it. Finally, we manually create a mask that indicates the regions where ground truth depths can be obtained from the first capture, as shown in the third row of Figure 5.

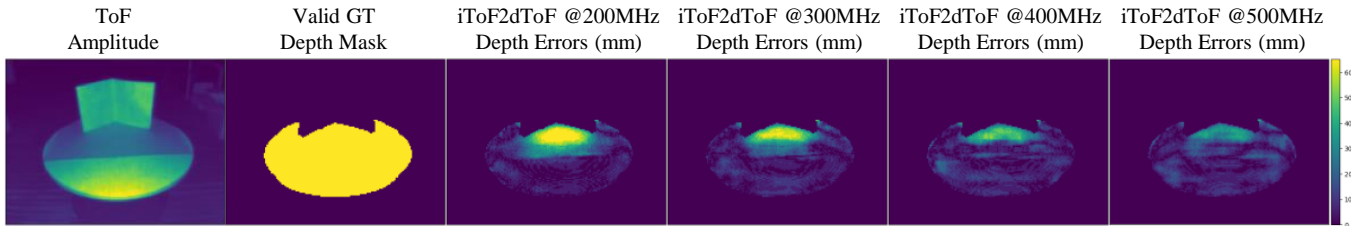


Supplementary Figure 5: **Real-world Depth Errors at 1ms Exposure Time.** Depth errors for iToF2dToF and two other data-driven baselines. Partial ground truth depths are obtained as described above in Section S. 4. The percentile MAE calculated for all models, over these scenes and the scenes in Section S. 7-B, is reported in Table 3 of the main document.

A. Real-world Quantitative Evaluation

Main Observations: Figure 5 shows the depth errors for a denoising network (iToF2iTof), an end-to-end network (iToF2Depth), and for iToF2dToF. iToF2dToF achieves the lowest depth errors in 6 out of 7 of the scenes. The only scene that iToF2dToF does not outperform iToF2Depth was in the ‘Dark Table Corner’ scene (4th column). There are two explanations for this result. First, these corner-like scenes are well-represented in the dataset, which as we have discussed, is the ideal case for end-to-end models like iToF2Depth. And second, as we observe in Figure 6, 400MHz may not be a high enough frequency to completely mitigate MPI in this scenario. Nonetheless, iToF2dToF was able to consistently achieve lower depth errors in the more complex scenes (columns 5-7). In the Appendix we show the results for these scenes using 0.5ms, 0.2ms, and 0.1ms exposure times. In these lower exposure settings, the performance of iToF2dToF degrades gracefully, and the dominant errors start being due to noise and not MPI.

Summary: Our quantitative evaluation shows that data-driven methods, trained on synthetic data only, have the capability to generalize to real-data. Although, iToF2dToF does achieve the lowest percentile MAE computed over the 28 instance test set we captured, we also observed the strengths of an end-to-end model, like iToF2Depth, in scene configurations that were well-represented in the synthetic dataset. Finally, as we decreased the SNR (exposure time), iToF2dToF’s performance degraded gracefully as seen in the Appendix Figures 18, 19, 20.

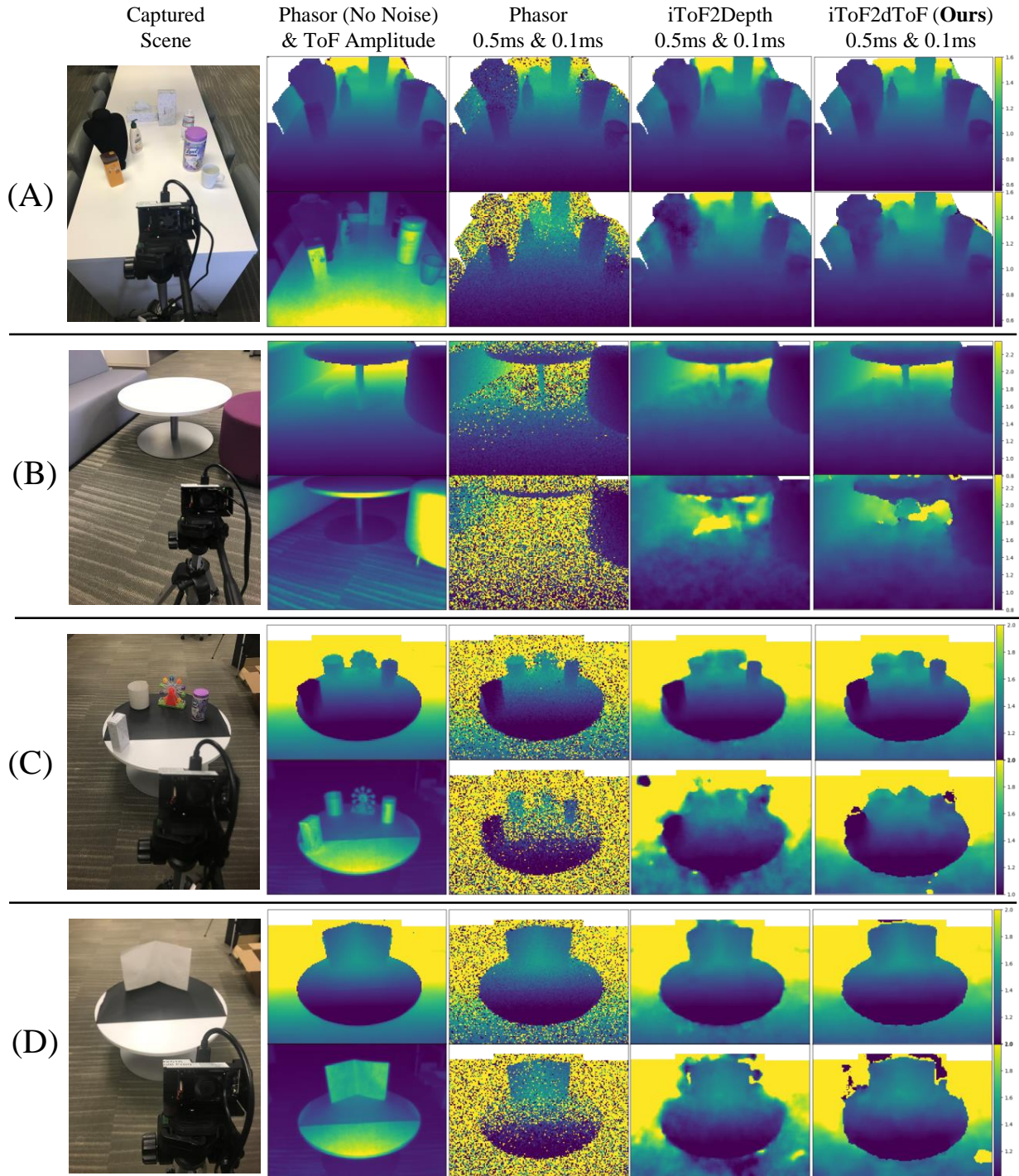


Supplementary Figure 6: Effect of Max Frequency in iTof2dToF Depth Errors. As we increase the maximum frequency used in iTof2dToF, the depth errors due to MPI decrease.

B. Extremely Low SNR Depth Reconstruction

Main Observations: Figures 7 and 21 show the depth images reconstructed by different methods at very low exposure times (0.1ms-1ms). At extremely low SNR, (e.g., 0.1ms or 0.2ms), all depth images contain some artifacts. However, we observe that even at such low exposure times, iTof2dToF, is able to estimate accurate depths in some regions, and overall displays fewer artifacts than other models.

Summary: In this section, we evaluated iTof2dToF at extremely low exposure times and empirically verified that the quality of the reconstructed depth maps degraded gracefully.



Supplementary Figure 7: Extreme Low SNR Depth Reconstructions. Recovered depths for multiple scenes at low exposure times (0.5ms and 0.1ms). The Phasor (No Noise) images provide an approximate view of how the correct depth image should look like. The Phasor depth images (3rd column) does not apply any denoising to the data, and it is a useful image to identify low and high SNR regions. For visualization purposes, we mask pixels (white regions) that exhibit phase wrapping or that were still noisy in the “noiseless” Phasor image. We find that even at extremely low exposure times, iToF2dToF, is still able to recover accurate depths in some regions of the image.

S. 5. ADDITIONAL REAL-WORLD RESULTS

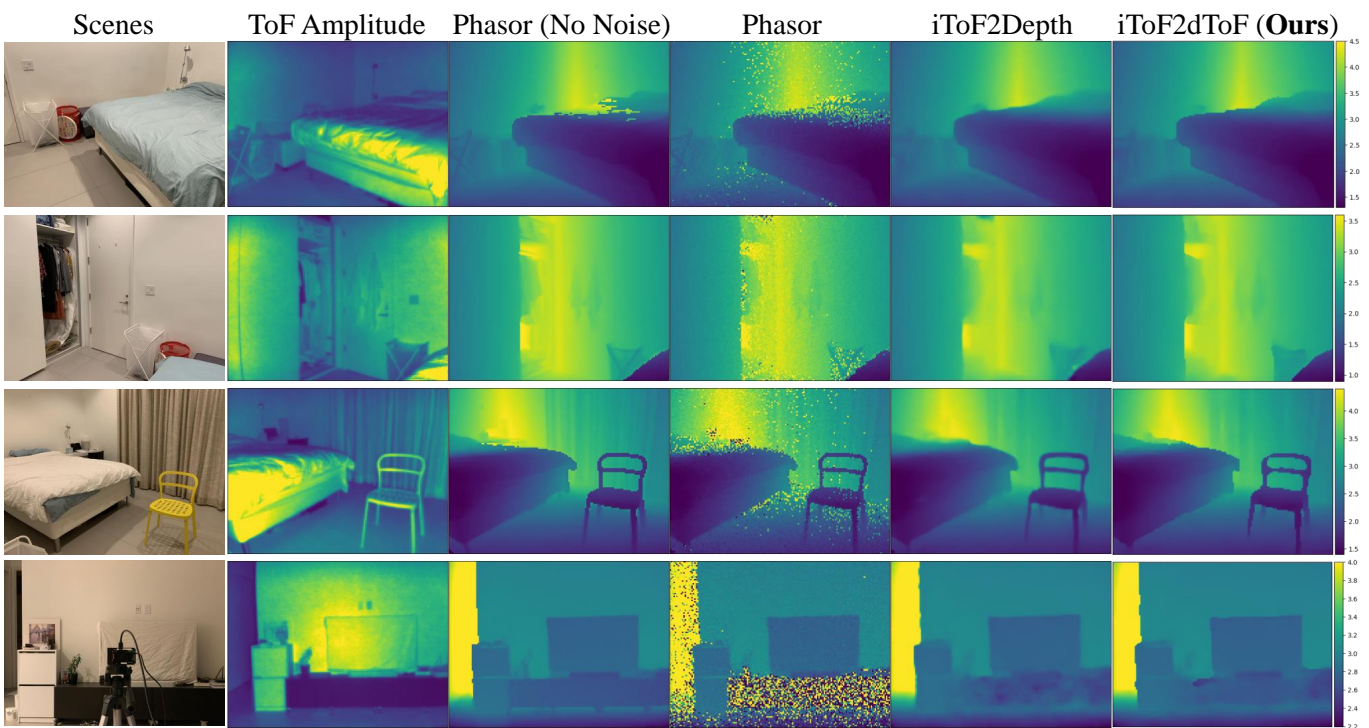
A. Additional Qualitative Depth Reconstructions

In this section we present additional qualitative depth reconstructions for everyday real-world scenes. Despite the unavailability of ground truth depth in these scenes, we draw some useful observations from the quality of the reconstructions.

Main Observations: Figure 8 shows the estimated depths by iToF2dToF and some of the baselines established in the main paper. The data-driven methods recover depth maps that are comparable to the traditional method Phasor (No Noise) in most regions with high enough SNR, indicating good generalization. We point out two specific points in the depth reconstructions:

- **Low SNR Artifacts:** Low SNR regions can be identified by looking at the 4th column, the depth maps of the Phasor method without any denoising. In the bottom row, in extreme low SNR regions, the performance of data-driven methods degrades gracefully resulting in some artifacts. Nonetheless, in other low SNR regions the data-driven methods and iToF2dToF in particular, produce reliable depth estimates.
- **Edges in Depth Images:** In low-resolution images, depth discontinuities (edges) will look different across methods because they are dealt with differently. In iToF2Depth, the network is trained to predict flying pixels, because that is what the ground truth says. In iToF2dToF, we use a peak finding depth estimation algorithm so the depth will depend on the peak that is chosen between the background and foreground. Similar to iToF2dToF, Phasor, uses a look-up table algorithm. However, due to the low temporal resolution of the look-up table, the peaks of background and foreground blend, resulting again in flying pixels. Ultimately, these differences will be highly mitigated in higher resolution images. Please refer to Section S. 5-C for a follow-up analysis of this situation.

Summary: Overall, data-driven methods trained on synthetic data appear to generalize well to real data, despite the modeling assumptions made when simulating the synthetic data. They are able to mitigate strong MPI (top row) and degrade gracefully at low SNR (bottom row).



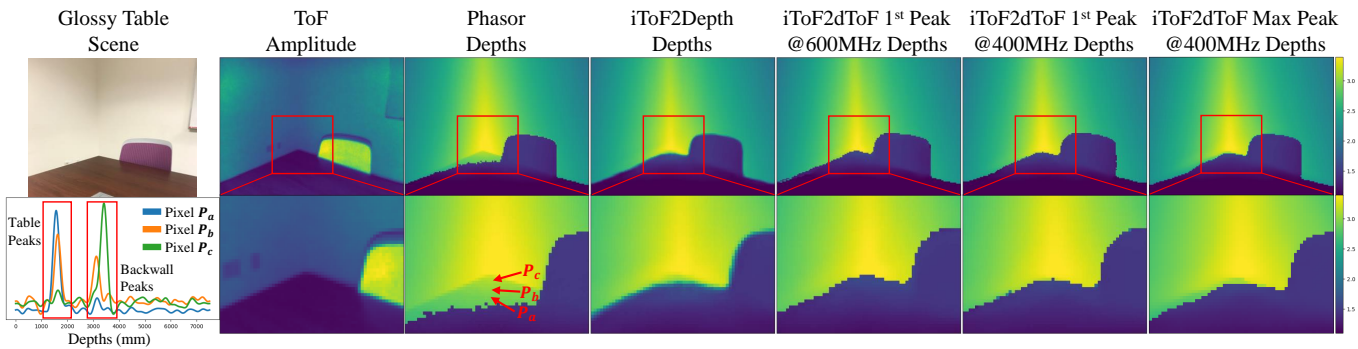
Supplementary Figure 8: **Real-world Depth Images.** Recovered depths by iToF2dToF and some of the baseline established in the main document. All scenes were acquired using a 1ms exposure time per frame. The Phasor (No Noise) is obtained by averaging 100 iToF frames and then compute depths using the phasor method, so it has minimal noise and can give us an approximate view of the ground truth depths. Both data-driven methods (iToF2Depth and iToF2dToF) exhibit good generalization and recover high-quality depth maps. *Zoom in for better visualization.*

B. Additional Specular MPI Correction Result

In this section we present the depth reconstruction of a glossy table that exhibits semi-specular reflections. We use the same first peak finding algorithm for iToF2dToF that was described in the specular MPI section of the main document.

Main Observations: The data-driven methods (iToF2Depth and iToF2dToF) are less susceptible than the Phasor method to depth errors caused by the specular reflections on the glossy table, as shown in Figure 9. Although, iToF2Depth recovers accurate depths in the less specular regions of the table, it starts predicting erroneous depths in the more specular regions located towards the corner of the table. This is expected because, as observed in transient pixel P_c , the direct reflection for these pixels is weak. Finally, using iToF2dToF with a 1st peak finding algorithm results in the most accurate reconstruction. However, the pixels right at the corner of the table are too specular, which results in iToF2dToF choosing the specular peak as the correct peak. Interestingly, in this example, we found it beneficial to use the iToF2dToF model trained to extrapolate up to 600MHz.

Summary: When imaging complex materials, by analyzing the dToF representation, we can design appropriate peak finding algorithms that can result in higher-quality depth reconstructions. Furthermore, in this example there appears to be a small benefit in extrapolating to a higher frequency. Exploring methods and the benefits of extrapolating to higher frequencies is an interesting direction for future work.



Supplementary Figure 9: **Glossy Table Depth Reconstruction.** The first row shows the estimated depths of the scene. The second row shows the zoomed in depth maps in the regions that displayed strong specular MPI. In the first column of the first row, we plot 3 transient pixels produced by iToF2dToF. As illustrated in the Phasor depth image, the selected transient pixels correspond to highly glossy points on the table. Pixel P_a has a strong 1st peak and weak 2nd peak, while pixel P_c has a weak 1st peak and strong 2nd peak. In these pixels the correct depth corresponds to the 1st peak. This results in iToF2dToF 1st peak (5/6th columns) producing a more accurate depth map than iToF2dToF Max Peak (7th column). *If possible, zoom in for details like the ‘glossiness’ of the table, the improvements in the depth reconstruction, and the reconstructed transient pixels.*

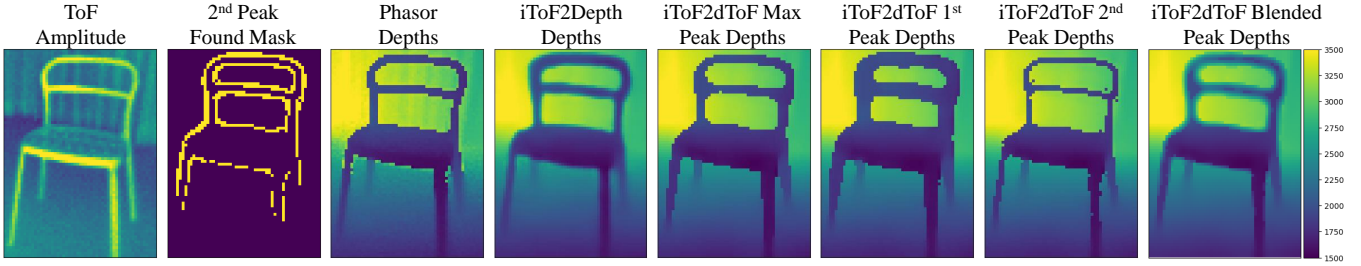
C. Depth Image Refinement

In this section we analyze the differences on the depth image edges across different methods. These differences are mainly applicable to low-resolution images, like the ones used in this paper, and as the resolution increases these differences might become negligible.

Main Observations: Figure 10 compares the recovered depth maps across different methods. The depth predicted for edge pixels varies across methods. iToF2Depth produces depths that blur the foreground and background (flying pixels). iToF2dToF, depending on the peak finding algorithm, can choose the foreground (1st peak), the background (2nd peak), somewhere in between (blended peaks), or the peak with highest intensity (max peak). Ultimately, the correct depth for an edge pixel is ambiguous and may depend on the application. For instance,

- **Obstacle Avoidance:** Consider a robot vacuum using depth images from an iToF camera to navigate a living room. In this scenario, a depth image where the object edges are dilated, as in iToF2dToF 1st peak, might be beneficial to ensure that the vacuum avoids the objects.
- **Robotic Grasping** Consider a robotic hand picking up objects. In order to ensure a tight grasp of the object it may be beneficial to use a depth image with thinned edges such as iToF2dToF 2nd peak.

Summary: The correct depth for an edge pixel will most likely be determined by the application. In iToF2dToF, we can adjust the depth estimation algorithm to either choose the foreground depth (first peak) or background depth (second peak) depending on the scenario. This is another example of the benefits of estimating a flexible intermediate representation. Nonetheless, as we increase the depth image resolution these edge differences across methods may become negligible and possibly irrelevant.

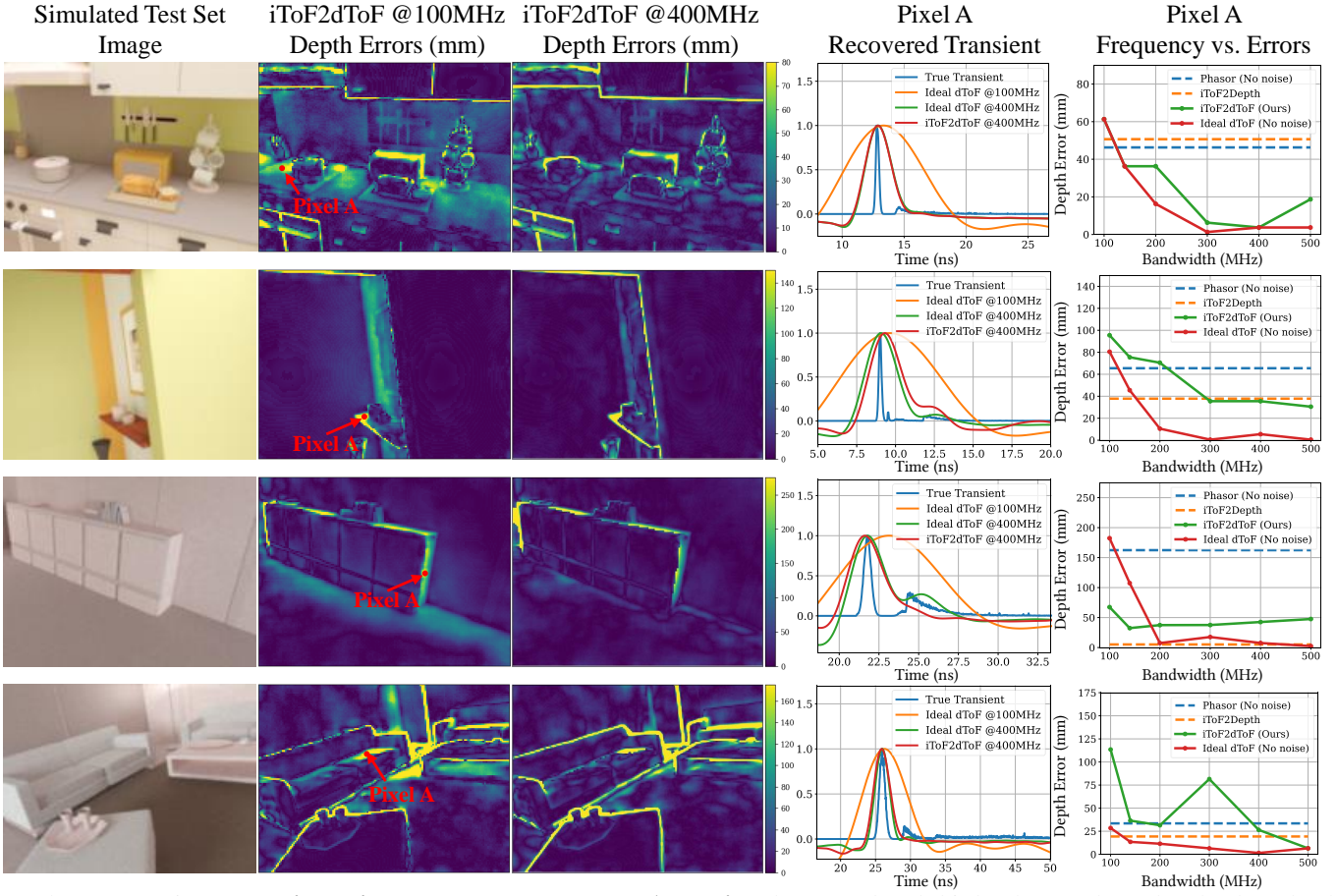


Supplementary Figure 10: **Depth Image Edge Comparison.** For Phasor, iToF2Depth, and iToF2dToF Max Peak we use the depth estimation algorithms that have been used throughout the paper. For iToF2dToF 1st peak, we use the same algorithm that was used for specular MPI correction. For iToF2dToF 2nd peak, we compute edges with a canny edge detector on the ToF amplitude image, take the max peak depth image, and replace the depths at edge pixels with the 2nd peak depths. To find the 2nd peak we use the same peak finding algorithm described for specular MPI. Finally, for iToF2dToF blended peaks, we do a weighted averaging of the 1st and 2nd peak depth images, where the weights are determined by the peak heights.

S. 6. ADDITIONAL SYNTHETIC DATA RESULTS

A. Pixel-wise Frequency Analysis

In this section we compare the depth errors obtained by iToF2dToF models that extrapolate to 100MHz and 400MHz. Furthermore, we show different transient pixels reconstructed by iToF2dToF and compare them to the ideal dToF case. The ideal dToF reconstructions are obtained using the ground truth frequency data we use to train iToF2dToF.



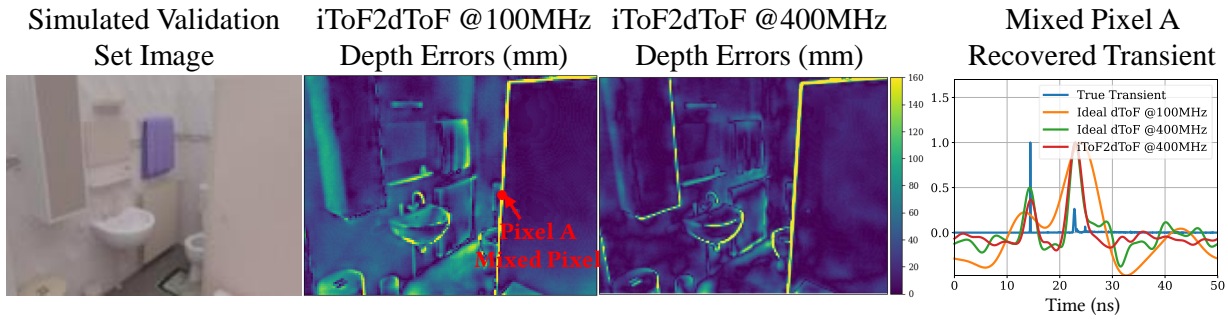
Supplementary Figure 11: Pixel-wise Error and Frequency Analysis. The second and third columns show the absolute depth errors in 4 different test set scenes. For each scene, we also plot one transient pixel (fourth column) reconstructed by iToF2dToF @400MHz. In the transient pixel plots only iToF2dToF contains noise. The true and ideal dToF transient pixels do not have noise. Finally, in the last column, we plot the depth errors of that single pixel for various models as a function of frequency. The performance of the Phasor and iToF2Depth baselines does not depend on frequency. On the other hand, for the iToF2dToF and the ideal dToF models, there is a clear trend of errors decreasing as we increase frequency.

Main Observations: Figures 11 and 12 compare the depth errors of iToF2dToF at different maximum frequencies. An iToF2dToF model only interpolating frequencies up to 100MHz (second column), continues to exhibit large depth errors due to MPI. Extrapolating up to 400MHz mitigates these errors to a large extent (third column). To understand the effect of frequency on performance we look at iToF2dToF’s transient pixel reconstructions (fourth column), in the following cases:

- **Non-Sparse MPI:** As observed in the fourth column of Figure 11, even for an ideal dToF transient pixel with frequencies up to 100MHz (orange line), the non-sparse MPI observed in the true transient (blue line), causes a significant bias in the maximum peak’s location. This bias is largely mitigated if we include frequencies up to 400MHz (green line). Despite the presence of noise in iToF2dToF’s input, the model is able reconstruct transient pixels (red line) that resemble the ideal dToF case.
- **Sparse MPI at Edges:** The fourth column of Figure 12 shows the reconstruction of the transient pixel at a depth discontinuity (edge). As discussed in Sections S. 5-A and S. 5-C the ground truth depth for these pixels is ambiguous. Nonetheless, learning to estimate the correct transient waveform for these sparse transient pixels is still important. And as shown in Figure 12, iToF2dToF’s capability to estimate the sparse peak locations is comparable to the ideal dToF case.
- **Failure Case:** The third row in Figure 11 shows one transient pixel reconstruction that led to elevated depth errors. Although, iToF2dToF does a reasonable approximation of the transient pixel, the peak has a small bias to the left. This particular transient pixel was challenging to reconstruct at all frequencies, as seen in the depth errors plotted in the last

column. This failure could be caused by extremely low SNR levels for those pixels, or insufficient generalization by iToF2dTof. The latter can be easily solved by increasing the dataset size or using more complex architectures and training procedures like the ones proposed in previous works.

Summary: Overall, there is a clear relationship between the depth accuracy of a ToF system and its bandwidth (maximum frequency). Our results show that, data-driven iToF-based transient imaging methods, like iToF2dTof, can extrapolate to higher frequencies and effectively increase the bandwidth of the system. Interestingly, the depth errors, in the ideal dToF case, plateau around 400MHz (red line in last column of Figure 11). This empirical finding is consistent with previous analysis on the performance of iToF systems as a function of frequency [1], [15]. Furthermore, this suggests that future work should not solely focus on extrapolating to higher frequencies, but also focus on improving the quality of the transient reconstructions. One simple approach to achieve this could be to input 3-4 frequency measurements, which continues to be practical. It is important to note that the maximum frequency required to resolve MPI will depend on the scale of the scene [1], and our analysis has largely focused on indoor scenes where iToF cameras are most often used.



Supplementary Figure 12: **Sparse Transient Example.** The second and third columns show the absolute depth errors for one validation set scene. The last column plots the sparse transient waveforms for an edge pixel. iToF2dTof is able to accurately estimate the sparse peak locations.

B. Incorporating Amplitude Information

We find that using amplitude information helps improve the performance of all models on synthetic data. Unfortunately, without the use of extensive calibration [7] or more complex architectures and learning procedures [8, 44], the models trained with amplitude information do not generalize well to real data. In this section, we compare the performance on synthetic data of models trained with and without amplitude, and also show the failure case on real data. Furthermore, we show that the robustness of iToF2dToF to noise continues to hold when amplitude information is added.

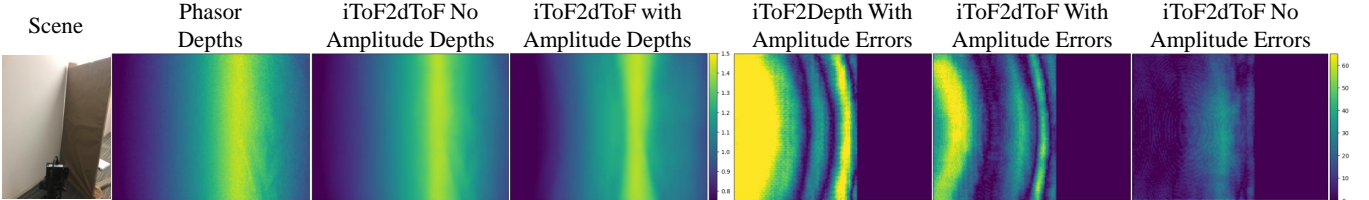
Similar to our setup in the main paper, the inputs to the networks are dual-frequency iToF measurements at 20 and 100MHz. Instead of normalizing each frequency measurement by its own amplitude, we normalize all frequencies by dividing by the lowest frequency amplitude. The amplitude ratio across frequencies is known to contain useful information about MPI [37], and has been used as an input in previous data-driven ToF models [44]. However, for the input frequencies we find that the ratio makes training less stable due to an increased number of divisions by 0 due to noise. To resolve this we apply light gaussian smoothing ($\text{stddev} = 0.5\text{px}$) on the input amplitudes, which stabilized training and improved performance.

Main Observations: Table V shows performance of the different models evaluated in the paper with and without amplitude information. Providing amplitude as input improves the performance of all models. Furthermore, Figure 13 shows a similar trend in which the performance gap between of iToF2dToF and iToF2Depth widens as we lower SNR. Therefore, we expect that the results we show in this paper will continue to hold if we incorporate amplitude information as input. Unfortunately, as observed in Figure 14 the data-driven models trained with amplitude information do not perform well on real-data.

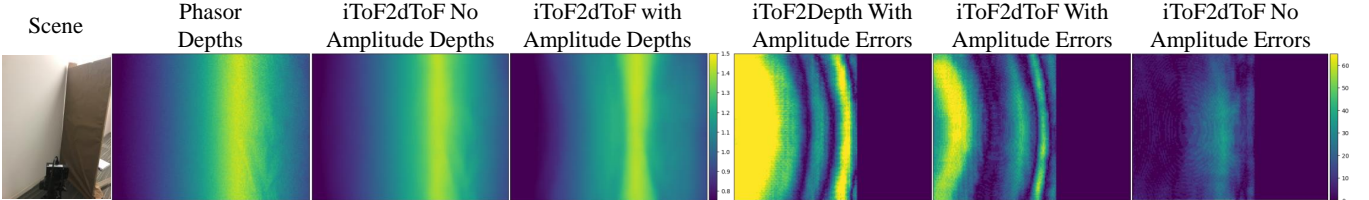
Summary: Overall, providing amplitude information as part of the input to the data-driven model is beneficial for all the methods we evaluate. The challenge arises in the generalization to real data. Certain non-idealities in the hardware or calibration errors, lead to large depth errors in the learned models.

Model	Synthetic Test Set Percentile MAE (mm)			
	0-75%	75-85%	85-95%	95-99%
Phasor (No Noise) [1]	9.53	29.58	46.37	94.79
iToF2Depth [3]	7.49	21.86	34.99	88.03
iToF2Depth w/ Amp.	7.35	21.27	33.66	81.76
iToF2dToF @200MHz	7.85	23.26	36.69	78.60
iToF2dToF @200MHz w/ Amp	7.03	21.60	34.79	75.77
iToF2dToF @400MHz	7.19	20.42	32.18	71.56
iToF2dToF @400MHz w/ Amp	6.24	18.20	29.68	69.30
iToF2dToF @500MHz	7.22	20.40	32.17	72.12
iToF2dToF @500MHz w/ Amp	6.19	17.92	29.52	69.88
iToF2dToF @600MHz	7.33	20.66	32.76	76.13
iToF2dToF @600MHz w/ Amp	6.26	18.17	30.02	70.93

TABLE V: Percentile MAE calculated over the test set simulated over a wide range of SNR levels. All models benefit from being trained with amplitude. Furthermore, we continue to see that iToF2dToF performance plateaus around 400MHz, even if we train with amplitude information



Supplementary Figure 13: **Noise vs. Error on Synthetic Test Set.** We simulate the same test set at multiple SNR levels. As we lower SNR, we continue to see a widening in the performance gap between iToF2dToF and iToF2Depth when amplitude is used.

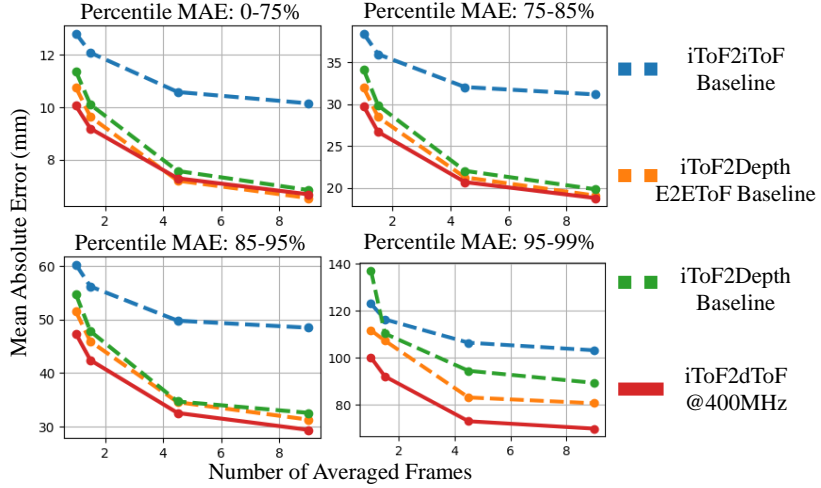


Supplementary Figure 14: **Real-world Result of Models Trained with Amplitude Information.** We test the data-driven models trained with amplitude information as described above on one of our real-world scenes with partial ground truth. The depth errors obtained by the data-driven models trained with amplitude information (5th and 6th columns) are significantly higher than a model not trained without amplitude information in the input (last column). Furthermore, the errors appear to be systematic (note the periodicity) which might suggest that they are due to imperfect calibration.

C. Increasing Network Size

In this section, we compare iToF2dToF with an additional iToF2Depth model that uses a larger network. This iToF2Depth model uses the same architecture as [3], where 9 residual layers are added between the encoding and decoding stages of the U-net. This results in a model with 12.495M parameters, which is $\sim 7x$ more parameters than the other data-driven models in this paper. We refer to this model as *iToF2Depth-E2EToF*, and train it in the exact same way as iToF2Depth.

Main Observations: Figure 15 shows that using a larger network for iToF2Depth helps improve overall performance and its robustness to noise. Nonetheless, despite using $\sim 7x$ more parameters, the performance of iToF2Depth-E2EToF continues to be worse than iToF2dToF. Lighter-weight networks that use less memory and require less computations, such as the one used for iToF2dToF and most of the baselines, are desirable in mobile applications where iToF cameras are often used.



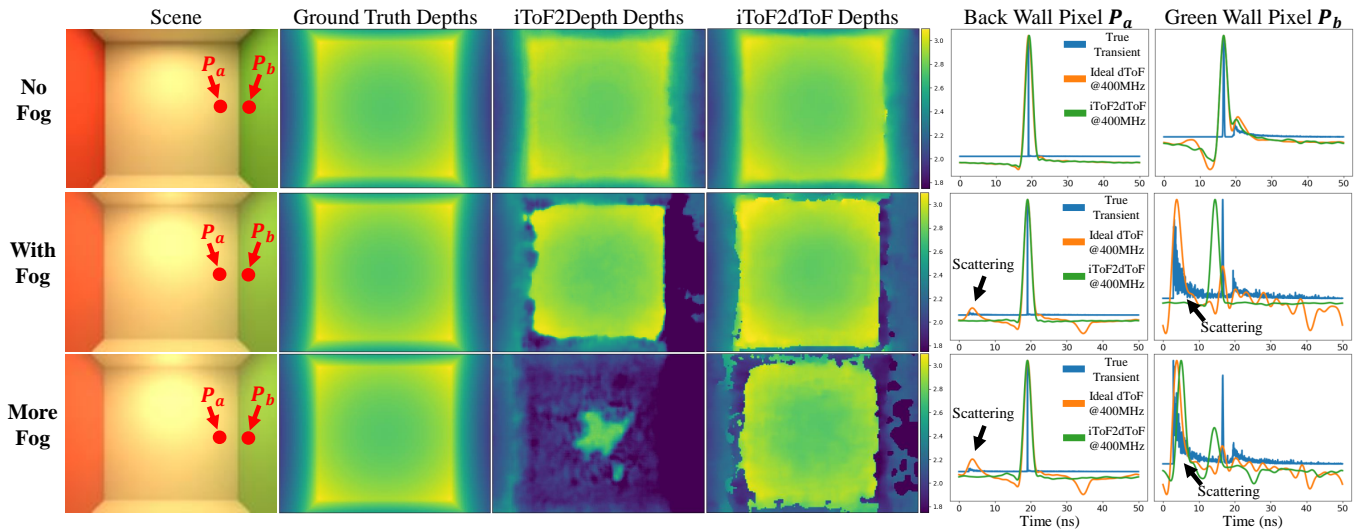
Supplementary Figure 15: Noise vs. Error on Synthetic Test Set. We simulate the same test set at multiple SNR levels as described in Section S. 2-B. Each model was trained with images containing the full range of SNR levels. For all SNR levels, iToF2dToF outperforms all baselines. In particular, as we reduce the number of frames (reduce SNR) the performance gap between iToF2dToF and the end-to-end models widens. At the lowest SNR settings, iToF2Depth performs comparably or worse than a simple denoising network (iToF2iToF). Using a larger model, like E2EToF, helps improve the robustness to noise of the end-to-end model, at the expense of using $\sim 7x$ more parameters.

D. Does iToF2dToF Generalize to Scattering Media?

In this section we evaluate the generalization capabilities of the data-driven models to a scene with different levels of fog density. Depths in iToF2dToF are reconstructed using the maximum peak.

Main Observations: Figure 16 shows the depth reconstruction by iToF2Depth and iToF2dToF in the presence of fog. iToF2Depth completely breaks at the highest fog level, while iToF2dToF continues to reconstruct the back wall. However, the estimated transient pixels by iToF2dToF do not faithfully approximate the ideal dToF transient in the presence of fog (second and third rows). In the scene without fog (first row), we can see that iToF2dToF does a good job in approximating the ideal dToF transient. However, as we introduce fog, which drastically changes the true transient and the ideal dToF transient, iToF2dToF stops matching the ideal dToF. Interestingly, at the highest level of fog (3rd row) in the green wall pixel P_b (last column), iToF2dToF does a more reasonable job. One possible explanation could be that, in this case, the scattering peak is higher than the direct reflection peak, and iToF2dToF interprets this scenario as sparse MPI.

Summary: Complex light transport events caused by scattering media are not well represented in our synthetic dataset. This prevents iToF2dToF from producing an accurate estimate of the transient pixels. Nonetheless, iToF2dToF does display some robustness to these out-of-distribution examples when compared to iToF2Depth. An interesting direction for future work is to explore methods that will enable data-driven transient imaging methods, like iToF2dToF, to generalize to these more complex light transport events.

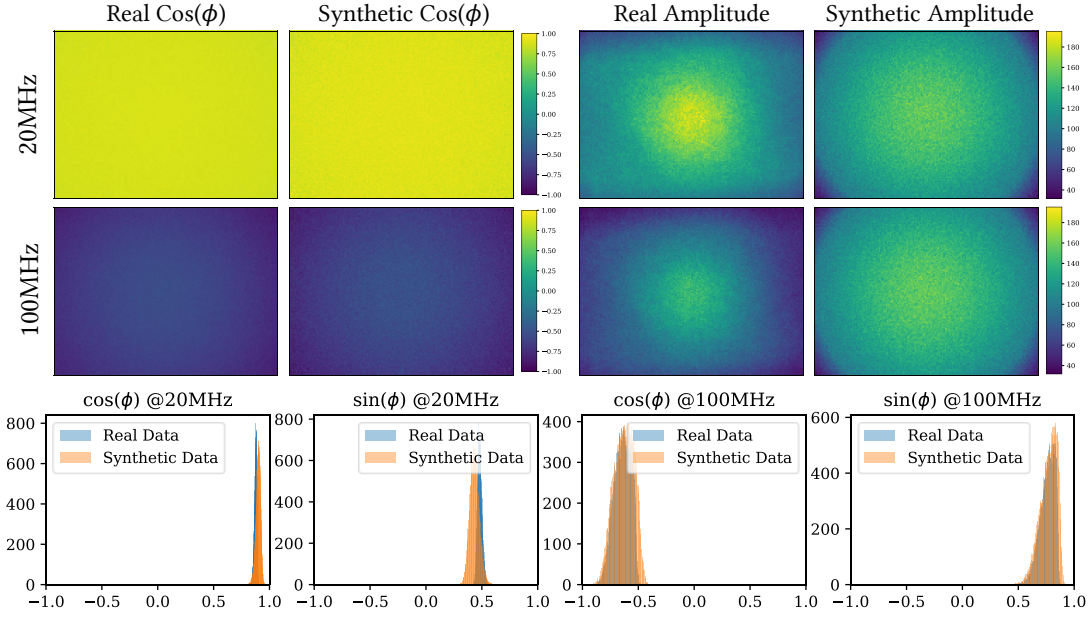


Supplementary Figure 16: **Fog Simulation Results.** The first row shows the reconstructed depths for the scene without fog. The second and third rows show the reconstructed depths for the same scene simulated with 2 fog density levels. The amount of scattering due to the fog can be observed in the transient pixels plotted in the last two columns. The green wall pixel P_b has a very low reflectivity, so the signal due to scattering is comparable to the reflected signal from the wall. *If possible, zoom in to observe the scattering signal in the transient pixels, in particular the white wall pixel P_a .*

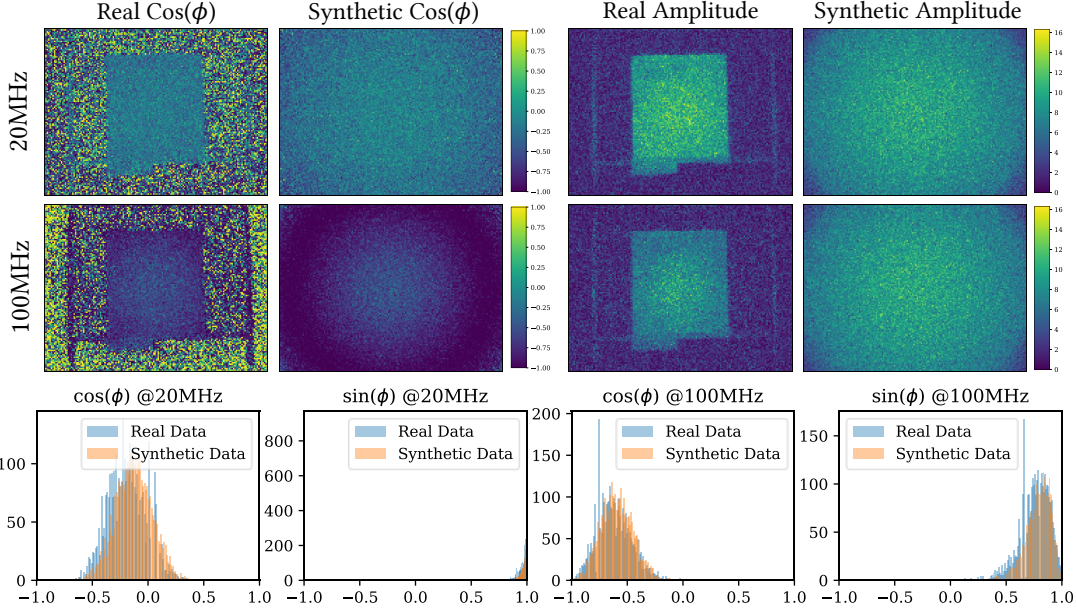
S. 7. APPENDIX

A. Appendix: Additional Simulator Validation Figures

Real vs. Synthetic Data of a Flat Wall 500mm Away

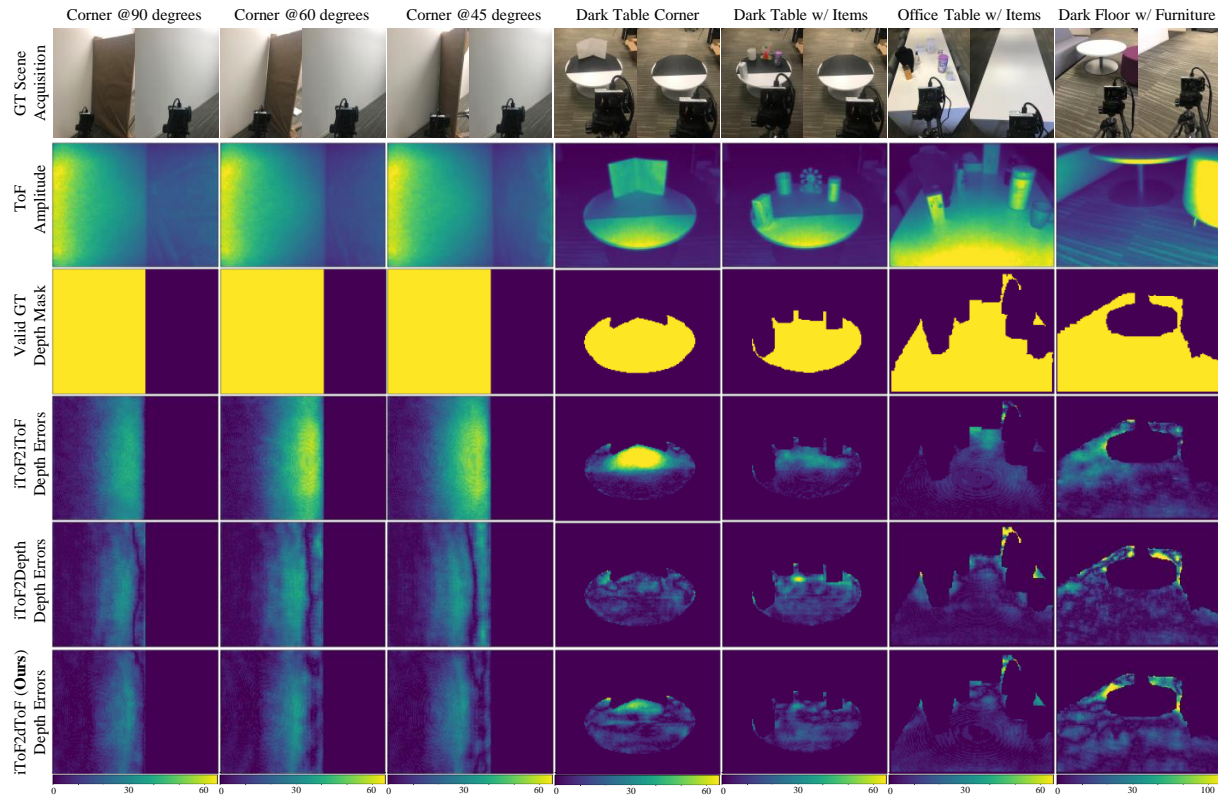


Real vs. Synthetic Data of a Flat Wall 2000mm Away

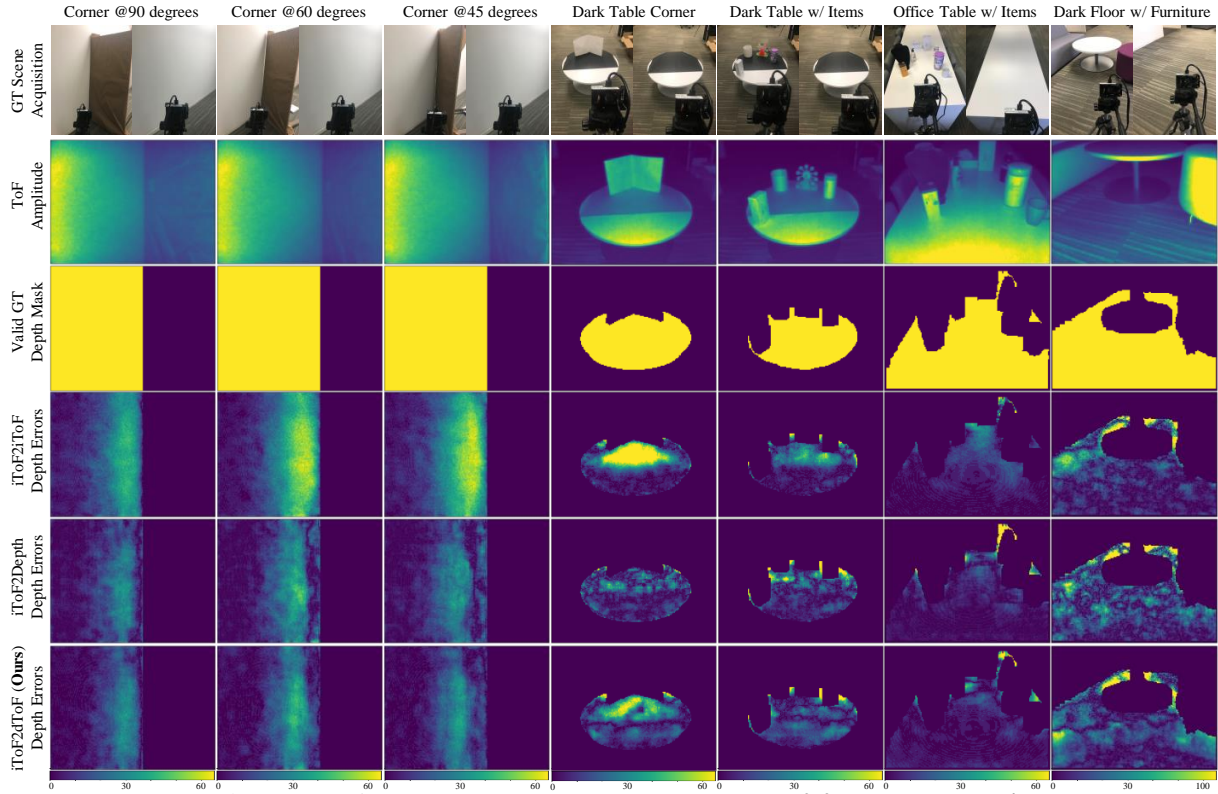


Supplementary Figure 17: **Synthetic vs. Real ToF Images** of a flat wall 500mm and 2000mm away from the camera. The first row shows the real and synthetic phase images (columns 1 and 2), and the real and synthetic amplitude images (columns 3 and 4), for 20MHz. The second row shows the same images, but for 100MHz. The flat plain used to capture the above real images did not cover the complete field of view of the camera, as seen in the real phase and amplitude images. Therefore, when calculating the distribution of the recovered phases (third row), we cropped the real and synthetic images such that we only included the valid pixels.

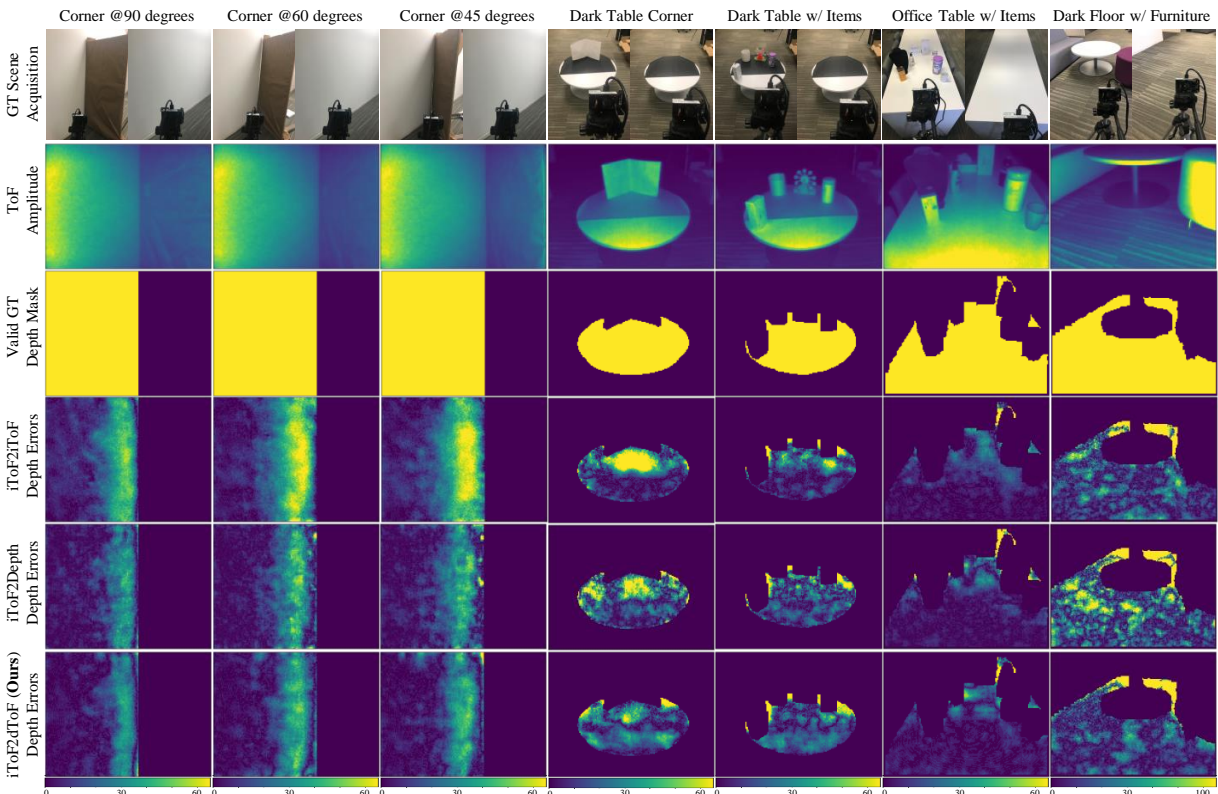
B. Appendix: Additional Real-world Quantitative Depth Errors



Supplementary Figure 18: **Real-world Depth Errors at 0.5ms Exposure Time.**

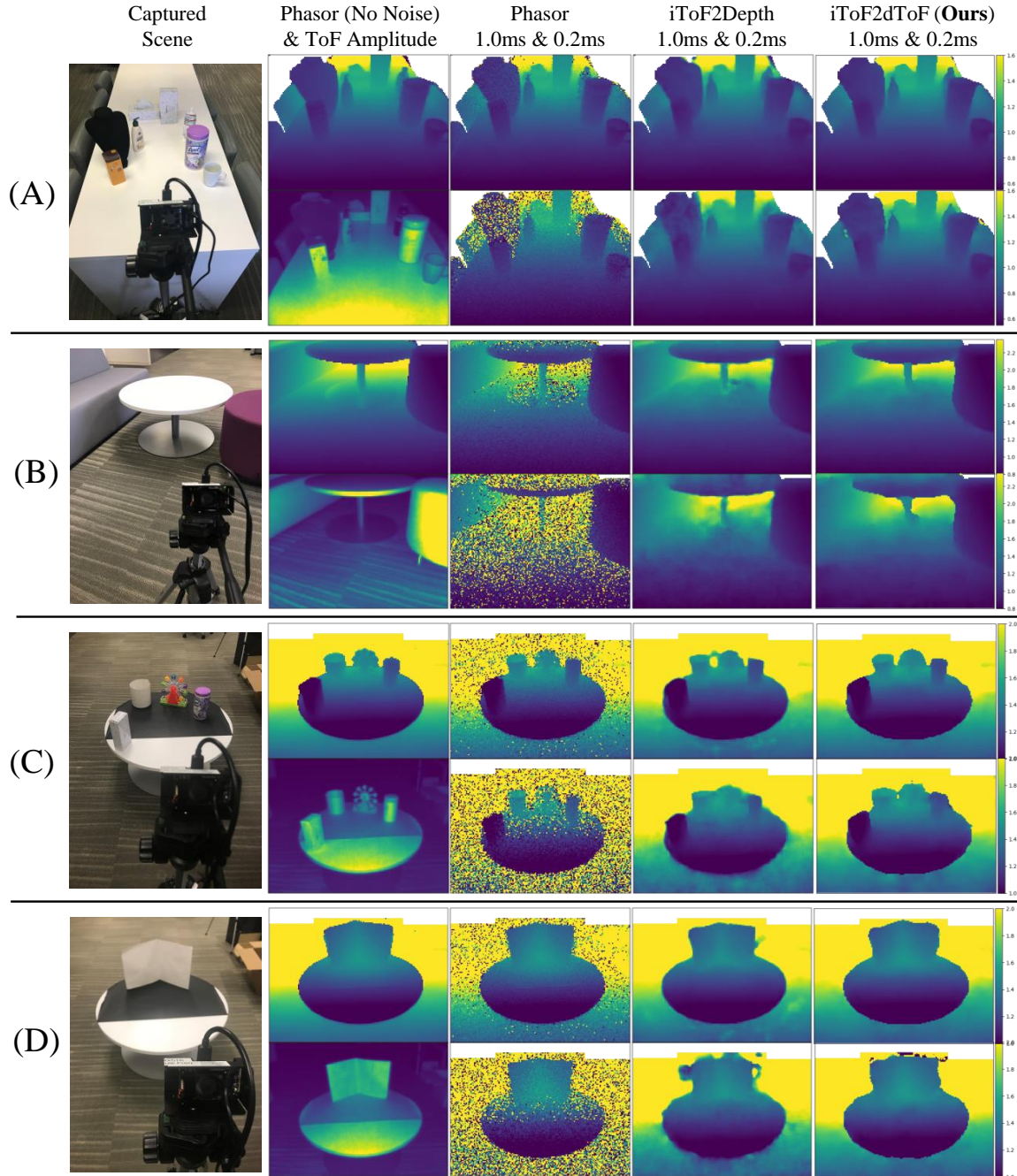


Supplementary Figure 19: Real-world Depth Errors at 0.2ms Exposure Time.



Supplementary Figure 20: Real-world Depth Errors at 0.1ms Exposure Time.

C. Appendix: Additional Extreme Low SNR Depth Reconstructions



Supplementary Figure 21: **Extreme Low SNR Depth Reconstructions.** Recovered depths for multiple scenes at low exposure times (1.0ms and 0.2ms). The Phasor (No Noise) images provide an approximate view of how the correct depth image should look like. The Phasor depth images (3rd column) does not use apply any denoising to the data, and it is a useful image to identify low and high SNR regions. For visualization purposes, we mask pixels (white regions) that exhibit phase wrapping or that were still noisy in the “noiseless” Phasor image. We find that even at extremely low exposure times iToF2dTof is still able to recover accurate depths in some regions of the image.

REFERENCES

- [1] M. Gupta, S. K. Nayar, M. B. Hullin, and J. Martin, "Phasor imaging: A generalization of correlation-based time-of-flight imaging," *ACM Transactions on Graphics (ToG)*, vol. 34, no. 5, p. 156, 2015. [2](#), [6](#), [7](#), [15](#), [16](#)
- [2] F. Gutierrez-Barragan, S. A. Reza, A. Velten, and M. Gupta, "Practical coding function design for time-of-flight imaging," in *Proceedings of the IEEE Conference on Computer Vision and Pattern Recognition*, 2019, pp. 1566–1574. [1](#), [2](#), [4](#), [6](#)
- [3] S. Su, F. Heide, G. Wetzstein, and W. Heidrich, "Deep end-to-end time-of-flight imaging," in *Proceedings of the IEEE Conference on Computer Vision and Pattern Recognition*, 2018, pp. 6383–6392. [1](#), [2](#), [4](#), [5](#), [6](#), [7](#), [16](#), [17](#)
- [4] R. Lange and P. Seitz, "Solid-state time-of-flight range camera," *IEEE Journal of quantum electronics*, vol. 37, no. 3, pp. 390–397, 2001. [1](#), [3](#)
- [5] Y. Chen, J. Ren, X. Cheng, K. Qian, L. Wang, and J. Gu, "Very power efficient neural time-of-flight," in *The IEEE Winter Conference on Applications of Computer Vision*, 2020, pp. 2257–2266. [1](#), [3](#)
- [6] J. Marco, Q. Hernandez, A. Munoz, Y. Dong, A. Jarabo, M. H. Kim, X. Tong, and D. Gutierrez, "Deeptof: off-the-shelf real-time correction of multipath interference in time-of-flight imaging," *ACM Transactions on Graphics (ToG)*, vol. 36, no. 6, p. 219, 2017. [1](#), [2](#), [4](#), [5](#), [6](#)
- [7] Q. Guo, I. Frosio, O. Gallo, T. Zickler, and J. Kautz, "Tackling 3d of artifacts through learning and the flat dataset," in *Proceedings of the European Conference on Computer Vision (ECCV)*, 2018, pp. 368–383. [1](#), [2](#), [4](#), [5](#), [8](#), [16](#)
- [8] G. Agresti, H. Schaefer, P. Sartor, and P. Zanuttigh, "Unsupervised domain adaptation for tof data denoising with adversarial learning," in *Proceedings of the IEEE Conference on Computer Vision and Pattern Recognition*, 2019, pp. 5584–5593. [1](#), [2](#), [4](#), [5](#), [16](#)
- [9] D. Qiu, J. Pang, W. Sun, and C. Yang, "Deep end-to-end alignment and refinement for time-of-flight rgb-d module," in *Proceedings of the IEEE International Conference on Computer Vision*, 2019, pp. 9994–10003. [1](#), [2](#), [8](#), [4](#)
- [10] Y. Cheng, D. Wang, P. Zhou, and T. Zhang, "A survey of model compression and acceleration for deep neural networks," *arXiv preprint arXiv:1710.09282*, 2017. [1](#)
- [11] A. G. Howard, M. Zhu, B. Chen, D. Kalenichenko, W. Wang, T. Weyand, M. Andreetto, and H. Adam, "Mobilenets: Efficient convolutional neural networks for mobile vision applications," *arXiv preprint arXiv:1704.04861*, 2017. [1](#)
- [12] D. Wu, A. Velten, M. O'toole, B. Masia, A. Agrawal, Q. Dai, and R. Raskar, "Decomposing global light transport using time of flight imaging," *International journal of computer vision*, vol. 107, no. 2, pp. 123–138, 2014. [1](#), [2](#)
- [13] P. Mirdehghan, W. Chen, and K. N. Kutulakos, "Optimal structured light à la carte," in *Proceedings of the IEEE Conference on Computer Vision and Pattern Recognition*, 2018, pp. 6248–6257. [1](#), [4](#)
- [14] S. Achar, J. R. Bartels, W. L. Whittaker, K. N. Kutulakos, and S. G. Narasimhan, "Epipolar time-of-flight imaging," *ACM Transactions on Graphics (TOG)*, vol. 36, no. 4, p. 37, 2017. [2](#), [6](#)
- [15] A. Kadambi, J. Schiel, and R. Raskar, "Macroscopic interferometry: Rethinking depth estimation with frequency-domain time-of-flight," in *Proceedings of the IEEE Conference on Computer Vision and Pattern Recognition*, 2016, pp. 893–902. [2](#), [15](#)
- [16] N. Naik, A. Kadambi, C. Rhemann, S. Izadi, R. Raskar, and S. Bing Kang, "A light transport model for mitigating multipath interference in time-of-flight sensors," in *Proceedings of the IEEE Conference on Computer Vision and Pattern Recognition*, 2015, pp. 73–81. [2](#)
- [17] M. O'Toole, F. Heide, L. Xiao, M. B. Hullin, W. Heidrich, and K. N. Kutulakos, "Temporal frequency probing for 5d transient analysis of global light transport," *ACM Transactions on Graphics (ToG)*, vol. 33, no. 4, p. 87, 2014. [2](#)
- [18] G. Agresti and P. Zanuttigh, "Combination of spatially-modulated tof and structured light for mpi-free depth estimation," in *Proceedings of the European Conference on Computer Vision (ECCV)*, 2018, pp. 0–0. [2](#)
- [19] R. Whyte, L. Streeter, M. J. Cree, and A. A. Dorrrington, "Resolving multiple propagation paths in time of flight range cameras using direct and global separation methods," *Optical Engineering*, vol. 54, no. 11, p. 113109, 2015. [2](#)
- [20] M. Gupta, A. Velten, S. K. Nayar, and E. Breitbach, "What are optimal coding functions for time-of-flight imaging?" *ACM Transactions on Graphics (TOG)*, vol. 37, no. 2, p. 13, 2018. [2](#)
- [21] A. Adam, C. Dann, O. Yair, S. Mazor, and S. Nowozin, "Bayesian time-of-flight for realtime shape, illumination and albedo," *IEEE transactions on pattern analysis and machine intelligence*, vol. 39, no. 5, pp. 851–864, 2017. [2](#), [6](#)
- [22] A. Velten, D. Wu, A. Jarabo, B. Masia, C. Barsi, C. Joshi, E. Lawson, M. Bawendi, D. Gutierrez, and R. Raskar, "Femto-photography: capturing and visualizing the propagation of light," *ACM Transactions on Graphics (ToG)*, vol. 32, no. 4, p. 44, 2013. [2](#)
- [23] M. O'Toole, F. Heide, D. B. Lindell, K. Zang, S. Diamond, and G. Wetzstein, "Reconstructing transient images from single-photon sensors," in *Proceedings of the IEEE Conference on Computer Vision and Pattern Recognition*, 2017, pp. 1539–1547. [2](#)
- [24] A. Raghuram, A. Pediredla, S. G. Narasimhan, I. Gkioulekas, and A. Veeraraghavan, "Storm: Super-resolving transients by oversampled measurements," in *2019 IEEE International Conference on Computational Photography (ICCP)*. IEEE, 2019, pp. 1–11. [2](#)
- [25] R. Warburton, C. Aniculaesei, M. Clerici, Y. Altmann, G. Gariepy, R. McCracken, D. Reid, S. McLaughlin, M. Petrovich, J. Hayes *et al.*, "Observation of laser pulse propagation in optical fibers with a spad camera," *Scientific reports*, vol. 7, p. 43302, 2017. [2](#)
- [26] A. Gupta, A. Ingle, and M. Gupta, "Asynchronous single-photon 3d imaging," in *Proceedings of the IEEE International Conference on Computer Vision*, 2019, pp. 7909–7918. [2](#)
- [27] F. Heide, S. Diamond, D. B. Lindell, and G. Wetzstein, "Sub-picosecond photon-efficient 3d imaging using single-photon sensors," *Scientific reports*, vol. 8, no. 1, pp. 1–8, 2018. [2](#)
- [28] A. Lyons, F. Tonolini, A. Boccolini, A. Repetti, R. Henderson, Y. Wiaux, and D. Faccio, "Computational time-of-flight diffuse optical tomography," *Nature Photonics*, vol. 13, no. 8, pp. 575–579, 2019. [2](#)
- [29] S. Chan, A. Halimi, F. Zhu, I. Gyongy, R. K. Henderson, R. Bowman, S. McLaughlin, G. S. Buller, and J. Leach, "Long-range depth imaging using a single-photon detector array and non-local data fusion," *Scientific reports*, vol. 9, no. 1, pp. 1–10, 2019. [2](#)
- [30] J. Lin, Y. Liu, M. B. Hullin, and Q. Dai, "Fourier analysis on transient imaging with a multifrequency time-of-flight camera," in *Proceedings of the IEEE Conference on Computer Vision and Pattern Recognition*, 2014, pp. 3230–3237. [2](#), [6](#)
- [31] J. P. Godbaz, M. J. Cree, and A. A. Dorrrington, "Closed-form inverses for the mixed pixel/multipath interference problem in amcw lidar," in *Computational Imaging X*, vol. 8296. International Society for Optics and Photonics, 2012, p. 829618. [2](#)
- [32] A. Kirmani, A. Benedetti, and P. A. Chou, "Spumic: Simultaneous phase unwrapping and multipath interference cancellation in time-of-flight cameras using spectral methods," in *2013 IEEE International Conference on Multimedia and Expo (ICME)*. IEEE, 2013, pp. 1–6. [2](#)
- [33] C. Peters, J. Klein, M. B. Hullin, and R. Klein, "Solving trigonometric moment problems for fast transient imaging," *ACM Transactions on Graphics (TOG)*, vol. 34, no. 6, pp. 1–11, 2015. [2](#), [3](#), [4](#), [6](#)
- [34] A. A. Dorrrington, J. P. Godbaz, M. J. Cree, A. D. Payne, and L. V. Streeter, "Separating true range measurements from multi-path and scattering interference in commercial range cameras," in *Three-Dimensional Imaging, Interaction, and Measurement*, vol. 7864. International Society for Optics and Photonics, 2011, p. 786404. [2](#)
- [35] A. Kadambi, R. Whyte, A. Bhandari, L. Streeter, C. Barsi, A. Dorrrington, and R. Raskar, "Coded time of flight cameras: sparse deconvolution to address multipath interference and recover time profiles," *ACM Transactions on Graphics (ToG)*, vol. 32, no. 6, p. 167, 2013. [2](#), [6](#)
- [36] A. Bhandari, M. Feigin, S. Izadi, C. Rhemann, M. Schmidt, and R. Raskar, "Resolving multipath interference in kinect: An inverse problem approach," in *SENSORS, 2014 IEEE*. IEEE, 2014, pp. 614–617. [2](#), [6](#)
- [37] D. Freedman, Y. Smolin, E. Krupka, I. Leichter, and M. Schmidt, "Sra: Fast removal of general multipath for tof sensors," in *European Conference on Computer Vision*. Springer, 2014, pp. 234–249. [2](#), [6](#), [16](#)

- [38] F. Heide, M. B. Hullin, J. Gregson, and W. Heidrich, "Low-budget transient imaging using photonic mixer devices," *ACM Transactions on Graphics (ToG)*, vol. 32, no. 4, p. 45, 2013. [2](#), [4](#), [6](#)
- [39] J. Lin, Y. Liu, J. Suo, and Q. Dai, "Frequency-domain transient imaging," *IEEE transactions on pattern analysis and machine intelligence*, vol. 39, no. 5, pp. 937–950, 2016. [2](#)
- [40] H. Wang, H. Qiao, J. Lin, R. Wu, Y. Liu, and Q. Dai, "Model study of transient imaging with multi-frequency time-of-flight sensors," *IEEE Transactions on Pattern Analysis and Machine Intelligence*, 2020. [2](#)
- [41] A. Jarabo, J. Marco, A. Muñoz, R. Buisan, W. Jarosz, and D. Gutierrez, "A framework for transient rendering," *ACM Transactions on Graphics (ToG)*, vol. 33, no. 6, p. 177, 2014. [2](#)
- [42] A. Jarabo, B. Masia, J. Marco, and D. Gutierrez, "Recent advances in transient imaging: A computer graphics and vision perspective," *Visual Informatics*, vol. 1, no. 1, pp. 65–79, 2017. [2](#)
- [43] A. Pediredla, A. Veeraraghavan, and I. Gkioulekas, "Ellipsoidal path connections for time-gated rendering," *ACM Transactions on Graphics (TOG)*, vol. 38, no. 4, pp. 1–12, 2019. [2](#), [4](#)
- [44] G. Agresti and P. Zanuttigh, "Deep learning for multi-path error removal in tof sensors," in *Proceedings of the European Conference on Computer Vision (ECCV)*, 2018, pp. 0–0. [2](#), [16](#)
- [45] R. Schwarte, Z. Xu, H.-G. Heinol, J. Olk, R. Klein, B. Buxbaum, H. Fischer, and J. Schulte, "New electro-optical mixing and correlating sensor: facilities and applications of the photonic mixer device (pmd)," in *Sensors, Sensor Systems, and Sensor Data Processing*, vol. 3100. International Society for Optics and Photonics, 1997, pp. 245–253. [3](#)
- [46] F. J. Harris, "On the use of windows for harmonic analysis with the discrete fourier transform," *Proceedings of the IEEE*, vol. 66, no. 1, pp. 51–83, 1978. [4](#)
- [47] W. Chen, P. Mirdehghan, S. Fidler, and K. N. Kutulakos, "Auto-tuning structured light by optical stochastic gradient descent," in *Proceedings of the IEEE/CVF Conference on Computer Vision and Pattern Recognition*, 2020, pp. 5970–5980. [4](#)
- [48] W. Jakob, "Mitsuba renderer," 2010. [4](#), [5](#), [2](#)
- [49] B. Bitterli, "Rendering resources," 2016. [5](#), [2](#)
- [50] L. Blend Swap, "Blend swap," <http://www.blendswap.com>, 2016. [5](#), [2](#)
- [51] O. Ronneberger, P. Fischer, and T. Brox, "U-net: Convolutional networks for biomedical image segmentation," in *International Conference on Medical image computing and computer-assisted intervention*. Springer, 2015, pp. 234–241. [5](#), [4](#)
- [52] A. Paszke, S. Gross, F. Massa, A. Lerer, J. Bradbury, G. Chanan, T. Killeen, Z. Lin, N. Gimelshein, L. Antiga *et al.*, "Pytorch: An imperative style, high-performance deep learning library," in *Advances in neural information processing systems*, 2019, pp. 8026–8037. [5](#), [4](#)
- [53] D. P. Kingma and J. Ba, "Adam: A method for stochastic optimization," *arXiv preprint arXiv:1412.6980*, 2014. [5](#), [4](#)
- [54] P. Virtanen, R. Gommers, T. E. Oliphant, M. Haberland, T. Reddy, D. Cournapeau, E. Burovski, P. Peterson, W. Weckesser, J. Bright, S. J. van der Walt, M. Brett, J. Wilson, K. J. Millman, N. Mayorov, A. R. J. Nelson, E. Jones, R. Kern, E. Larson, C. J. Carey, İ. Polat, Y. Feng, E. W. Moore, J. VanderPlas, D. Laxalde, J. Perktold, R. Cimrman, I. Henriksen, E. A. Quintero, C. R. Harris, A. M. Archibald, A. H. Ribeiro, F. Pedregosa, P. van Mulbregt, and SciPy 1.0 Contributors, "SciPy 1.0: Fundamental Algorithms for Scientific Computing in Python," *Nature Methods*, vol. 17, pp. 261–272, 2020. [7](#)
- [55] J. Mure-Dubois and H. Hügli, "Real-time scattering compensation for time-of-flight camera," in *International Conference on Computer Vision Systems: Proceedings (2007)*, 2007. [7](#)
- [56] C. S. Bamji, S. Mehta, B. Thompson, T. Elkhatib, S. Wurster, O. Akkaya, A. Payne, J. Godbaz, M. Fenton, V. Rajasekaran *et al.*, "Impixel 65nm bsi 320mhz demodulated tof image sensor with 3μm global shutter pixels and analog binning," in *2018 IEEE International Solid-State Circuits Conference-(ISSCC)*. IEEE, 2018, pp. 94–96. [8](#)
- [57] S. Su, F. Heide, R. Swanson, J. Klein, C. Callenberg, M. Hullin, and W. Heidrich, "Material classification using raw time-of-flight measurements," in *Proceedings of the IEEE Conference on Computer Vision and Pattern Recognition*, 2016, pp. 3503–3511. [8](#)
- [58] M. Pharr, W. Jakob, and G. Humphreys, *Physically based rendering: From theory to implementation*. Morgan Kaufmann, 2016. [2](#)
- [59] R. Glanz, "A comparison of physically based rendering systems," Favoritenstrasse 9-11/E193-02, A-1040 Vienna, Austria, Mar. 2018. [Online]. Available: </research/publications/2018/glanz-2017-pbrcomparison/>
- [60] B. Styperek and J. Francesc, "Mitsuba integration plugging," <https://www.mitsuba-renderer.org/plugins.html>, 2010. [2](#)